ACS Biomaterials SCIENCE & ENGINEERING

pubs.acs.org/journal/abseba

Article

Geometric Control of Cell Behavior by Biomolecule Nanodistribution

Jakub Pospíšil, Miloš Hrabovský, Dáša Bohačiaková, Zuzana Hovádková, Miroslav Jurásek, Jarmila Mlčoušková, Kamil Paruch, Šárka Nevolová, Jiri Damborsky, Aleš Hampl, and Josef Jaros*

Cite This: *ACS Biomater. Sci. Eng.* 2022, 8, 4789–4806

Read Online

ACCESS | Metrics & More | Article Recommendations | Supporting Information

ABSTRACT: Many dynamic interactions within the cell microenvironment modulate cell behavior and cell fate. However, the pathways and mechanisms behind cell−cell or cell−extracellular matrix interactions remain understudied, as they occur at a nanoscale level. Recent progress in nanotechnology allows for mimicking of the microenvironment at nanoscale *in vitro*; electron-beam lithography (EBL) is currently the most promising technique. Although this nanopatterning technique can generate nanostructures of good quality and resolution, it has resulted, thus far, in the production of only simple shapes (e.g., rectangles) over a relatively small area (100 × 100 μm), leaving its potential in biological applications unfulfilled. Here, we used EBL for cell-interaction studies by coating cell-culture-relevant material with electron-conductive indium tin oxide, which formed nanopatterns of complex nanohexagonal structures over a large area (500 × 500 μm). We confirmed the potential of EBL for use in cell-interaction studies by analyzing specific cell responses toward differentially distributed nanohexagons spaced at 1000, 500, and 250 nm. We found that our optimized technique of EBL with HaloTags enabled the investigation of broad changes to a cell-culture-relevant surface and can provide an understanding of cellular signaling mechanisms at a single-molecule level.

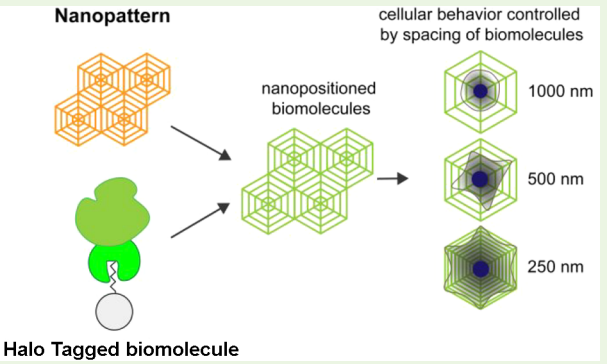

KEYWORDS: *nanopatterning, nanospacing, biomimetic surface, electron-beam lithography, cell−cell interaction, cell adhesion and spreading, ligand clustering*

INTRODUCTION

Cells of multicellular organisms continuously interact with their microenvironment, which contains soluble factors (e.g., growth factors), extracellular matrix (ECM) ligands (that control cell−ECM interactions), and surrounding cells (that control cell−cell interactions).[1−3] These interactions help regulate biological processes, coordinate cell behavior during development, contribute to the maintenance of tissue homeostasis, and control disease progression. In contrast to the expanding knowledge of regulatory circuits controlled by soluble factors, the molecular mechanisms behind cell−cell and cell−ECM interactions are unclear, and the effects of distribution and geometry of molecular interactors are particularly understudied.

Cell−cell and cell−ECM contacts underlie, at the macroscale level, the formation of tissue and barrier structures, whereas, at the microscale level, they drive signaling of specific pathways and activation states.[4] Cells are also sensitive to biochemical cues and geometric and mechanical constraints of their microenvironment, which are challenging to address *in vitro*, as cell culture surfaces are typically coated with ECM proteins in a random distribution.[5−8] Thus, to better control cell behavior, interactive molecules can be organized at the cell culture surface within defined microdomains.[9−11] These have been used to study cell migration, spread, adhesion, proliferation, and differentiation.[12−16] Nevertheless, most biologically relevant systems contain nanodistributed biomolecules, as many cell receptors and ligands naturally cluster into nanoscopic assemblies.[17] Nanodistribution can be achieved by nanopatterning, which controls the immobilization, arrangement, and density of ligands at the nanoscale level and which may help us understand how the spatial distribution of nanodistributed biomolecules affects signaling pathways.[18−21] Nanopatterning shows promise for applications such as nanobiochips, nanobiosensors for detection of disease biomarkers, and DNA nanosensors for drug screening.[22−24]

The key nanopatterning techniques appropriate for cell studies include dip-pen nanolithography, nanoshaving/nanografting, nanocontact printing, and electron-beam lithography

Received: June 6, 2022
Accepted: September 12, 2022
Published: October 6, 2022

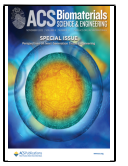

(EBL).[25−45] Each method has its advantages, disadvantages, and technological limitations for preparation; the critical parameters to be considered are the resolution of nanostructures (width in nm), throughput (total patterned area in μm^2), and shape complexity. Typically, structures with line widths greater than 50−1000 nm are fabricated; however, higher line resolution usually means exponentially longer preparation times and smaller patterned areas.[46] Additionally, many current techniques only produce simple shapes (e.g., lines and dots). Thus, EBL is currently the most promising technique for applications requiring high resolution and complex structures.[40] EBL is currently used for patterning biomolecules, such as DNA, antibodies, and other proteins, with structures up to 100 nm. However, only simple shapes have been generated (e.g., lines, crosses, and dots) over a relatively small area of 100 × 100 μm, which limits the scope of EBL to the study of approximately 10 cells.[43−45]

The current state of the art of bionanopatterning has led us to assume that the effective size of the patterned area for effective analysis of cellular interaction should be at least 400 × 400 μm. We also related the area size to human embryonic stem cells (hESC), used here as a model, that grow in colonies typically constituted by several hundred cells each. Such an average colony with 100 cells covers about 30 000 μm^2, which is equivalent to a colony diameter of about 100 μm. Finally, it was shown that proper recapitulation of embryonic processes by hESC grown on micropatterns is dependent on pattern size, with the minimal diameter being about 200 μm.[16,47] Thus, EBL has not yet fulfilled its potential to pattern complex structures with relevant biological throughput.

The specificity of signaling of immobilized molecules only in patterned regions is a challenge. *In vitro*, proteins adsorbed from media on culture surfaces may cause uncontrolled, nonspecific cell−surface interactions.[48] Nonspecific adsorption (NSA) occurs in all mentioned nanopatterning techniques and is typically solved with the addition of a protein nonfouling layer around the patterns.[49] Molecules, such as polyethylene glycol (PEG) and poly(2-hydroxyethyl methacrylate), have been used to create these nonadhesive regions. However, this approach when applied to nanopatterning must be optimized.[50]

A critical element required to create proper biodomain geometries is the anchoring of molecular moieties to prepared nanopatterns. Typically, this is achieved transiently by weak electrostatic binding or, for higher specificity, by bioaffinity binding (streptavidin−biotin) or permanently by strong covalent binding.[51−53] Recombinant proteins fused with HaloTags have allowed successful covalent immobilization of biomolecules on macrosurfaces.[54,55] HaloTag fusion proteins have high binding specificity toward surfaces via a thiol linker that forms a covalent bond with the target substrate. Many biomolecules can be tagged using HaloTag, making it a universal and widely applicable system.[56]

Biomolecule nanodistribution has been mainly used to target cell−ECM interactions by applying adhesive motifs from ECM proteins.[57] However, cell-cell interactions that also occur in nanoscopic assemblies remain understudied. Ephrin receptor tyrosine kinases (Eph receptors) and their ligands (ephrins) are promising candidates to study nanodistribution and cell−cell interactions. Eph receptors and ephrin ligands are membrane-bound proteins that require direct cell−cell interactions for activation and that regulate biological processes during embryonic development, such as cell migration, segmentation, and stem cell differentiation.[58−60] They must form highly organized nanoscopic clusters for effective signal transduction, which is affected by the distribution of binding partners within the membranes of neighboring cells. Indeed, the precise nanodistribution of the ligand ephrin A5 modulates ephrin type-A receptor 2 (EphA2) activity within cell membranes.[61] Notably, after ephrin binds an Eph receptor, the signal is transmitted bidirectionally, as the receptor and ligand are tethered in the cell membrane. Although Eph receptor signaling has been well studied, the downstream activity of ephrin ligands remains to be investigated.

Here, we optimized and implemented a biomolecule-based nanodistribution technique to develop a versatile tool for studying cell behavior. We used EBL to precisely distribute bioactive molecules in complex hexagonal patterns at a nanoscale level over a large area of 500 × 500 μm with high resolution and throughput, and we studied the effect of their distribution on cell attachment, cell spreading, and downstream signaling. We produced a hexagonal nanopattern of 100 nm wide lines spaced at 1000, 500, or 250 nm. The reasoning behind hexagons was as follows. Biologically, cells on planar culture surfaces spread in a circular shape.[62] When cells grow in colonies, they tile with no wasted area. The cells occupy the most efficient arrangement with the minimum perimeter over a given area. From a geometric point of view, an approximation of the cell shape that allows the tiling of regular patterns with equal size into a mosaic can be designed in three variants—triangles, squares, and hexagons. These shapes fold well together because they have straight edges that align with each other. The hexagon is closest to a circle, and its arrangement also appears very often in nature, e.g., six bonded carbon in organic chemistry, honeycomb, and compound eyes.[63] Then, we used a HaloTag-EphA2 (HT-EphA2) fusion protein to study the ability of our cellular model to interact with EphA2 anchored to the nanopatterns. We explored the effect of these interactions on cell behavior. Our results show specific interactions of human pluripotent stem cells (hPSCs) with nanodistributed EphA2 receptors and prove that cells respond to such distribution by changes to interactions with nanopatterns and ligand-driven activation of downstream signaling. Finally, our results demonstrate that this biomaterial can enable investigators to focus on broad changes to cell culture surfaces and can help us understand cell signaling mechanisms at a single-molecule level.

MATERIALS AND METHODS

Cleaning of Surfaces. We used 12 mm diameter high-precision cover glasses no. 1.5H (thickness = 170 μm ± 5 μm) for high-performance microscopes (cat. 0117520, Paul Marienfeld GmbH & Co. KG) to prepare patterned surfaces. Cover glasses were cleaned by sonication in methanol for 15 min and were washed three times for 15 min each in ultrapure Milli-Q water. Finally, the surfaces were dried in a flow of inert nitrogen gas.

Elimination of Nonspecific Adsorption by Polyethylene Glycol Modification. Each of the 97 PEG biomolecules that we tested (Table S1) was applied to the cleaned and dried surfaces as a 1 μL droplet, and the surfaces were incubated for 1 h at room temperature in a humidified chamber. Then, the PEG was removed by aspiration, and the surfaces were washed once with 0.1 M phosphate-buffered saline (PBS), pH 7.4. Finally, the HaloTag-fused protein was added, and the surfaces were incubated for 1 h at room temperature. The surfaces were incubated with primary antibody against the HaloTag (anti-HaloTag polyclonal antibody, cat. G9281, Promega) and subsequently with a secondary antibody conjugated to a

https://doi.org/10.1021/acsbiomaterials.2c00650
ACS Biomater. Sci. Eng. 2022, 8, 4789−4806

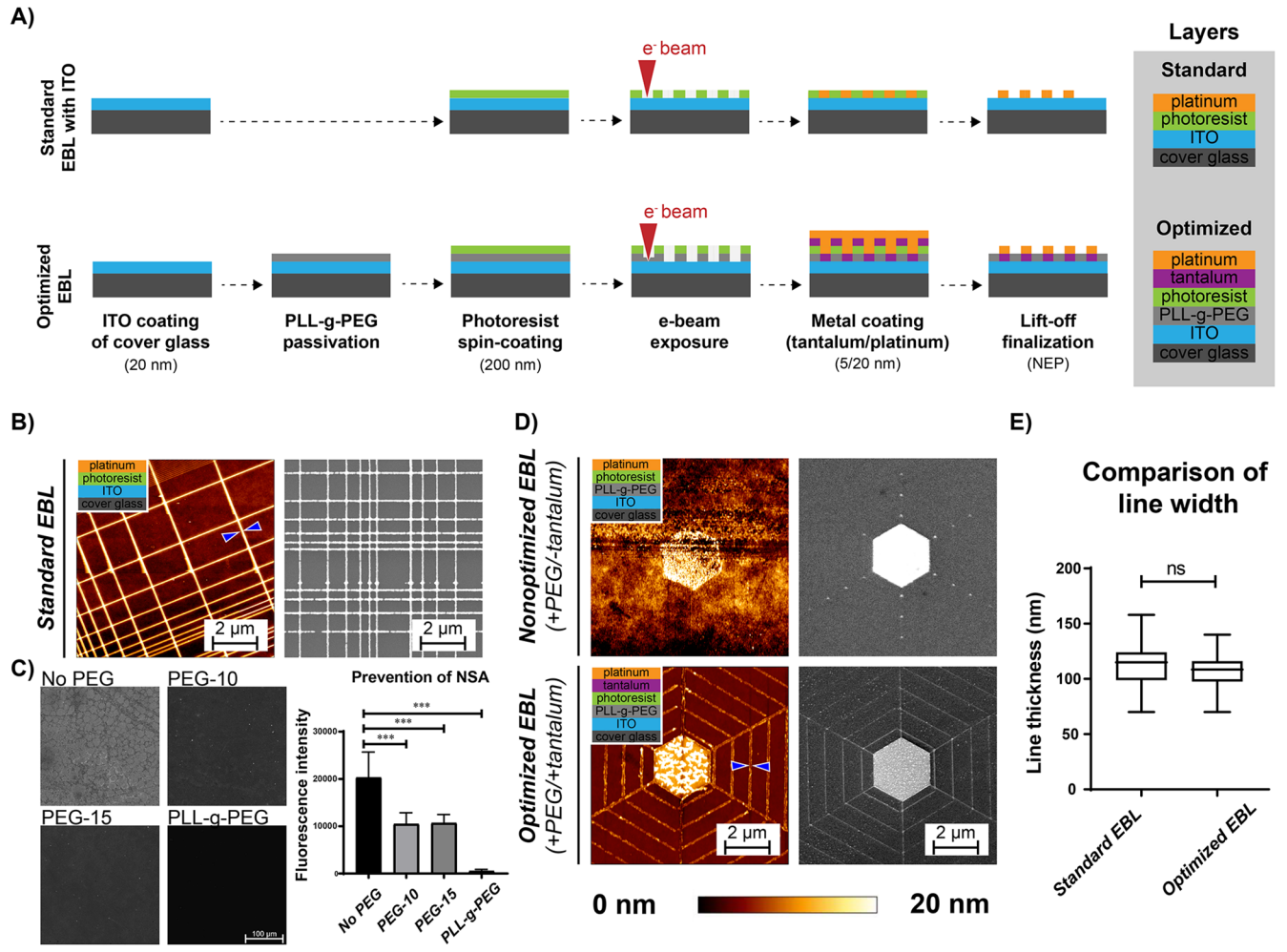

Figure 1. Optimization of electron-beam lithography workflow for cover glass substrates using PLL-g-PEG and tantalum layers. (A) Schematic illustration of standard and optimized EBL procedures combined with PLL-g-PEG and tantalum layers. Different colors represent different deposited layers, scale bar 2 μm. (B) AFM (left) and SEM (right) images of nanopatterns prepared by standard EBL with an ITO layer. A nanogrid with line spacings from 0.5 to 10 μm was produced on the surface without PEG and tantalum. (C) Immunofluorescence detection of HaloTag-fused biomolecules on ITO-coated surfaces treated with different PEG solutions to avoid NSA. The immunofluorescence intensity was quantified and graphed. Representative images (left) show NO PEG (sample without a PEG layer) and surfaces modified with PEG-10, PEG-15, and PLL-g-PEG. The effectiveness of each surface protein's repellent property was quantified as fluorescence intensity (right). Intensity measurements were performed in triplicate. From each sample replicate, 10 line sections were measured to obtain intensity values over the surface. Error bars represent ±standard error of the mean. (D) AFM (left) and SEM (right) characterization of PEG only (+PEG/−tantalum) and PEG and tantalum layers (+PEG/+tantalum) used for more complex nanohexagonal structures, scale bar 2 μm. (E) Quantification of AFM measurements of line width estimated as a full width at half-maximum. The mean line width achieved by standard EBL (−PEG/−tantalum) and optimized EBL (+PEG/+tantalum) was ∼100 nm (n = 50 cross-sections). Error bars represent ±standard error of the mean. Blue triangles illustrate locations where the cross-section measurements were taken. Image analyses were performed in ImageJ Fiji and software from JPK Instruments. The statistical analyses were performed using an unpaired t test. ***$p < 0.001$. ns, not significant.

fluorophore (Alexa Fluor 488, cat. A-11008, Invitrogen). To quantify the effectiveness of a variety of PEG solutions, we measured the immunofluorescence intensity of noncoated surfaces and PEG-coated areas of the surfaces and calculated the efficiency of passivation as a percentage.

Design of Macro-, Micro-, and Nanoscale Patterned Surfaces. For cell-interaction experiments, we designed three types of patterned surfaces with different scale precisions: MACRO (mm), MICRO (μm), and NANO (nm). The MACRO surface represents a simplified model with a large area of randomly immobilized HaloTag-fused recombinant proteins to fully support cell interactions. This surface served as confirmation of cell interactions with HaloTag-fused recombinant proteins and as a reference control. The MACRO surface comprises simple platinum circles (3 mm in diameter). MICRO patterned surfaces were designed as a field of filled hexagons with diameters of 2−40 μm and distances of 0.2−40 μm over a large area of 500 × 1000 μm. Hexagonal NANO patterns were produced with different spacings between lines (1000, 500, and 250 nm) in two variants without (NO CORE) or with (CORE) small, filled hexagonal centers. Our rationale for designing CORE hexagonal centers was to enhance cell-substrate interactions. We designed the parameters of the MICRO and NANO surfaces in the open-source software KLayout (https://www.klayout.de/), and the designs were exported to the Drawbeam/EBL kit of Atlas software (TESCAN Brno, s.r.o.).

Preparation of Platinum MACRO Surfaces. Cleaned cover glasses were sputter-coated with a 20 nm thick layer of indium tin oxide (ITO) using a Q150T S sputter coater (cat. 10027, Quorum Technologies) and a sputtering target (cat. EJTITOX57MM+, Kurt J. Lesker Co. Vacuum). The ITO-coated surfaces were PEGylated with PLL-g-PEG at 1 mg mL^{-1} for 1 h at room temperature, washed once

https://doi.org/10.1021/acsbiomaterials.2c00650
ACS Biomater. Sci. Eng. 2022, 8, 4789−4806

with 1× PBS, and left to dry. Finally, the circular macroscale pattern was achieved by platinum sputtering through a polydimethylsiloxane stencil mask (Alvéole) with a 3 mm diameter circular gap using a sputter coater (SCD 040, Oerlikon Balzers Ltd.) set at 30 mA for 2 min, which corresponds to a ∼20 nm line width.

Standard Electron-Beam Lithography by 30 keV Scanning Electron Microscopy. To test the potential of EBL for the preparation of NANO-patterned surfaces, we first performed a previously established workflow for EBL (standard EBL).[64] Cleaned surfaces were coated with a ∼20 nm thick layer of electron-conductive ITO. The coated surfaces were dehydrated and soft-baked at 150 °C for 60 s on an SD 160 vacuum hot plate (cat. 5510-4130, Cole-Parmer). Then, the first 20 μL of adhesion promoter AR 300-80 (Allresist GmbH) was spin-coated onto the surfaces at 500 rpm for 5 s and then ramped to 4000 rpm for 60 s. The surfaces were again soft-baked at 150 °C for 60 s, and 20 μL of electron-beam resist CSAR-6200 (AR-P 6200.09, Allresist GmbH) in a 9% anisole solution was spin-coated at 500 rpm for 5 s and then ramped to 4000 rpm for 60 s to form a ∼200 nm thick layer. Then, the surfaces had a final soft-baking at 150 °C for 90 s. EBL was performed on a Mira3 scanning electron microscope (TESCAN Brno, s.r.o.). Setup parameters for the MICRO pattern were an exposition with an acceleration voltage of 30 keV at a working distance of 9 mm, an absorption current of ∼330 pA, a step size of 24.4 nm, and a beam dose of 60 μC cm^{-2}. For the NANO pattern in the form of grid lines, the setup parameters were an acceleration voltage of 30 keV at a working distance of 9 mm, an absorption current of ∼330 pA, a step size of 12.2 nm, and a beam dose of 92 μC cm^{-2}. After EBL, the exposed parts of the electron-beam resist were treated with AR 600-546 (Allresist GmbH) for 60 s at room temperature. The entire surface was then coated with a ∼20 nm thick platinum layer using an SCD 040 sputter coater (Oerlikon Balzers Ltd.) for 2 min at 30 mA. The final step was the lift-off in *N*-ethyl pyrrolidone (NEP) solution, which resulted in the removal of the exposed resist layer and the production of hexagonal patterns. The NEP was removed by washing the slides in 40% isopropyl alcohol and then in Milli-Q water. The slides were dried in a flow of inert nitrogen gas and were ready for further procedures.

Optimized Electron-Beam Lithography. The optimized process of fabrication of nanopatterned surfaces by EBL is illustrated in Figure 1A. The optimized workflow was similar to the standard workflow. However, to eliminate nonspecific protein adsorption, it was necessary to add PLL-*g*-PEG (SuSoS Surface Technology). We incorporated a proadhesive tantalum layer for improved nanostructure cohesion of more complex hexagonal patterns. We have also slightly modified the hexagonal design, to which the thin (300 nm) interruption was added, to support the access of NEP solution during the lift-off process. Briefly, the optimized protocol was performed on cleaned surfaces coated with an ∼20 nm thick layer of electron-conductive ITO. Then, the surfaces were coated with a protein-repulsive layer composed of 1 mg mL^{-1} PLL-*g*-PEG (50 μL per cover glass) for 1 h at room temperature. Then, the PLL-*g*-PEG was removed by aspiration, and the surfaces were washed once with 1× PBS and left to dry. The surfaces were then dehydrated and soft-baked at 150 °C for 60 s on an SD 160 vacuum hot plate (cat. 5510-4130, Cole-Parmer). Then, 20 μL of adhesion promoter AR 300-80 (Allresist GmbH) was spin-coated onto the surfaces at 500 rpm for 5 s and then ramped to 4000 rpm for 60 s. The surfaces were soft-baked at 150 °C for 60 s, and 20 μL of electron-beam resist CSAR-6200 (AR-P 6200.09, Allresist GmbH) in a 9% anisole solution was spin-coated at 500 rpm for 5 s and then ramped to 4000 rpm for 60 s to form an ∼200 nm thick layer. Then, the surfaces had a final soft-baking at 150 °C for 90 s. EBL was performed on a Mira3 scanning electron microscope (TESCAN Brno, s.r.o.). Setup parameters for the nanopatterns were an acceleration voltage of 30 keV at a working distance of 9 mm, an absorption current of ∼330 pA, a step size of 12.2 nm, and a different beam dose for each density (92 μC cm^{-2} for 1000 nm, 88 μC cm^{-2} for 500 nm, and 86 μC cm^{-2} for 250 nm). After EBL, the exposed parts of the electron-sensitive resist were treated with AR 600-546 (Allresist GmbH) for 60 s at room temperature. To enhance the adhesiveness of the structures, we introduced a thin adhesive layer (∼5 nm) of tantalum (cat. EJTTAXX1.5A2, Kurt J. Lesker Co. Vacuum) to the EBL procedure using an SCD 040 sputter coater (Oerlikon Balzers Ltd.) prior to the addition of the platinum layer, which was applied using an SCD 040 sputter coater (Oerlikon Balzers Ltd.) for 2 min at 30 mA to produce an ∼20 nm thick platinum layer. The final step was the lift-off in NEP solution, which resulted in the removal of the exposed resist layer and the production of hexagonal patterns. The NEP was removed by washing the slides in 40% isopropyl alcohol and then in Milli-Q water. The slides were dried in a flow of nitrogen gas and were ready for further procedures.

Microscopy Characterization of Prepared Microscale and Nanoscale Surfaces. Patterned surfaces were characterized by SEM using a Mira3 scanning electron microscope and a VEGA microscope (TESCAN Brno, s.r.o.) and by AFM using a NanoWizard 3 instrument (JPK Instruments) and a Dimension FastScan instrument (Bruker) for high resolution. For AFM, the scanning frequency was set at 1 kHz for a resolution of 512 × 512 pixels and 0.5 kHz for a resolution of 1024 × 1024 pixels. The final images were processed and analyzed with SPM data processing software (JPK Instruments).

Immobilization of Proteins to Surfaces. Recombinant protein HT-EphA2 was incubated with a thiol linker (cat. P6761, Promega) for 1 h at 37 °C. The molar ratio of EphA2/linker was 100:1. The binding efficiency of the linker towards its specific epitope included in the HaloTag protein was confirmed by MALDI-TOF analysis. After linker binding, the entire protein complex was immobilized onto the patterned area of prepared surfaces as a 5 μL droplet (in 0.5 M trehalose and 1× PBS, pH 7.4) at 5 μg mL^{-1} at 37 °C for 1 h. Then, the unadsorbed protein was aspirated, and the surfaces were washed thoroughly three times in 1× PBS. All steps were performed immediately prior to cell seeding or immunofluorescence protein detection to avoid protein drying.

Immunofluorescence Detection of Immobilized Proteins. Proteins immobilized to patterns were detected by immunofluorescence microscopy using a polyclonal primary antibody against the HaloTag epitope of HT-EphA2 (anti-HaloTag, cat. G9281, Promega) and counterstaining with anti-rabbit secondary antibody conjugated to Alexa Fluor 488 (cat. A-11008, Invitrogen). Each antibody incubation was performed for 1 h at room temperature, and then, the surfaces were washed three times in 1× PBS. The samples were mounted using ProLong Gold antifade mountant (cat. P10144, Thermo Fisher Scientific). The samples were analyzed with an LSM880 laser scanning confocal microscope (Carl Zeiss AG) with a super-resolution Airyscan detector and with an Elyra 7 super-resolution structured illumination microscope (Carl Zeiss AG).

Culture of Human Pluripotent Stem Cells. We maintained hPSCs, also known as CCTL-14 (hPSCreg name: MUNIe007-A), in a hPSC medium on a supportive layer of mouse embryonic fibroblasts. The cell culture medium was composed of DMEM/F12 (cat. 21331020, Thermo Fisher Scientific), KnockOut serum replacement (cat. 10828028, Thermo Fisher Scientific), L-glutamine (cat. 25030024, Thermo Fisher Scientific), MEM nonessential amino acids (cat. 11140035, Thermo Fisher Scientific), penicillin−streptomycin (cat. 15070063, Thermo Fisher Scientific), 2-mercaptoethanol (cat. M3148, MilliporeSigma), and recombinant human FGF-basic (cat. 100−18B, PeproTech), as described previously.[65] For our experiments, the interaction of cells with the surface is restricted to the attachment of cells to one single biomolecule. Therefore, the hPSCs were also adapted to a fibroblast-free Matrigel cell culture system (Matrigel hESC-Qualified Matrix, cat. 356277, Corning). The hPSCs were propagated on this surface for at least 20 passages in mouse embryonic fibroblast-conditioned medium (hPSC medium supplemented with L-glutamine, FGF-basic, and secreted factors from mouse embryonic fibroblast cells) at 37 °C and 5% CO_2.

Real-Time Polymerase Chain Reaction. Gene expression of Eph receptors and ephrin ligands in hPSCs was evaluated by real-time polymerase chain reaction (PCR). Cells cultivated on Matrigel were lysed with Buffer RLT (Qiagen) for RNA isolation. The RNA was extracted using an RNeasy Mini kit (cat. 74104, Qiagen) and reverse transcribed using a Transcriptor First Strand cDNA synthesis kit (cat.

https://doi.org/10.1021/acsbiomaterials.2c00650
ACS Biomater. Sci. Eng. 2022, 8, 4789−4806

Table 1. Composition of Monomer Solution

component	stock concentration[a]	amount (mL)	final concentration[a]
sodium acrylate	38	2.25	8.6
acrylamide	50	0.5	2.5
N,*N*′-methylenebisacrylamide	2	0.75	0.15
sodium chloride	29.2	4	11.7
PBS (pH 7.4)	10×	1	1×
H_2O	n.a.[b]	0.9	n.a.
total		*9.4*	

[a]All concentrations in g 100 mL^{-1} except for PBS [b]n.a., not applicable.

04379012001, Roche). Real-time PCR was performed on a LightCycler 480 Instrument II system (cat. 05015278001, Roche) using the protocol for LightCycler 480 SYBR Green I master (cat. 04707516001, Roche). Designed primers supplied by Sigma-Aldrich are listed in Table S2.

Immunocytochemistry and Fluorescence Microscopy Analysis. Immunocytochemistry analysis was performed as previously described.[66] Briefly, the seeded cells were fixed in 4% paraformaldehyde for 15 min at room temperature. The cells were then permeabilized with 0.1% Triton X-100 detergent and subsequently blocked with 3% bovine serum albumin. The cells were washed three times in 1× PBS and labeled with primary antibodies, followed by secondary antibody staining. Primary and secondary antibodies were diluted in 3% bovine serum albumin (BSA; Sigma-Aldrich, St. Louis, MO) in PBS containing 0.05% Tween-20 (Sigma-Aldrich). The primary antibody was incubated overnight at 4 °C and the secondary for 60 min at room temperature. The nuclei were stained with 4′,6-diamidino-2-phenylindole, and the actin cytoskeleton was stained with rhodamine phalloidin (cat. R415, Thermo Fisher Scientific). The antibodies used in this study are listed in Table S3. Images were acquired with an LSM880 laser scanning confocal microscope (Carl Zeiss AG) with a super-resolution Airyscan detector and with an Elyra 7 super-resolution structured illumination microscope (Carl Zeiss AG).

Western Blot. Western blot analysis was performed as previously described.[67] Briefly, the cells were washed three times with PBS and lysed in lysis buffer (50 mM Tris-HCl pH 6.8, 1% sodium dodecyl sulfate, and 10% glycerol). The concentration of proteins was measured using the DC Protein Assay kit (BioRad), and the same amount of total protein (10 μg per lane) was separated using sodium dodecyl sulfate-polyacrylamide gel electrophoresis. The proteins were transferred onto polyvinylidene fluoride membranes (Millipore), and after blocking in 5% milk powder in Tris-buffered saline, the membranes were incubated overnight at 4 °C with the appropriate primary antibody (Table S3). Membranes were incubated with the horseradish peroxidase-conjugated secondary antibodies goat anti-rabbit (cat. G-21234, Thermo Fisher Scientific) or goat anti-mouse (cat. G-21040, Thermo Fisher Scientific), and the proteins were visualized on X-ray film (AGFA) using Amersham ECL Prime Western blotting detection reagent (GE Healthcare Life Sciences). Beta-actin was used as a loading control. The anti-beta-actin antibody (cat. ab6276, Abcam) was used to control for endogenous protein levels.

Seeding of Cells on Experimental Surfaces. Cells were harvested from Matrigel-coated cell culture dishes using enzymatic digestion with TrypLE Express enzyme (cat. 12605010, Thermo Fisher Scientific) and seeded at 26 600 cells cm^{-2} in mouse embryonic fibroblast-conditioned medium for all experimental surfaces (MACRO, MICRO, and NANO) with immobilized L-HT-EphA2 (5 μg mL^{-1}). To support cell spreading on nanoscale surfaces, hPSCs were seeded in a medium supplemented with 10 μM Y-27632, a Rho-associated protein kinase inhibitor (cat. SCM075, Sigma-Aldrich). The cells were fixed at time points that depended on the type of analysis. The cells were fixed after 24 h to confirm interaction of hPSCs with immobilized HaloTag protein on MACRO platinum surfaces (3 mm circles). The cells were fixed 4 h after seeding for cell-spreading analysis for different microdistributed biodomains. Cluster-distribution and cluster-volume analyses on nanosurfaces were performed on cells fixed 4 h after seeding. The nanosurface analysis of the ephrin A1 ligand dynamic was performed on cells fixed 30, 60, and 90 min after seeding.

Expansion Microscopy. The expansion procedure was performed as previously described for cell culture systems.[68] Briefly, hPSCs were seeded at 75 000 cells cm^{-2} on a circular macropatterned surface modified by L-HT-EphA2 or on a Matrigel layer. After 4 h, the cells were fixed with 4% paraformaldehyde, permeabilized with 0.1% Triton X-100 for 5 min at room temperature, and stained with antibodies, and the nuclei were counterstained, as described above for the immunofluorescence process. Subsequently, samples were incubated with 0.1 mg mL^{-1} acryloyl-X, SE (cat. A20770, Thermo Fisher Scientific), in 1× PBS overnight at room temperature. Unanchored acryloyl-X, SE, was removed by washing twice with 1× PBS for 15 min. Next, sample gelation was performed with a gelling solution containing 0.5% *N*,*N*,*N*′,*N*′-tetramethylethylenediamine (cat. T9281, Sigma-Aldrich) and 0.5% ammonium persulfate (cat. A3678, Sigma-Aldrich) for 30 min at 37 °C. The main gelling component is a monomer solution (Table 1) composed of sodium acrylate (cat. 408220, Sigma-Aldrich), acrylamide (cat. A8887, Sigma-Aldrich), *N*,*N*′-methylenebis(acrylamide) (cat. M7279, Sigma-Aldrich), and sodium chloride (cat. S6191, Sigma-Aldrich). Proteins and formed gels were subsequently denatured with proteinase K (8 U mL^{-1}; cat. EO0491, Thermo Fisher Scientific) in denaturing buffer at room temperature for at least 6 h (overnight denaturation was optimal). The composition of the denaturation buffer is listed in Table 2. The denaturation buffer contained Triton X-100 (cat. X100, Sigma-Aldrich), ethylenediaminetetraacetic acid (cat. BDH7830-1, VWR), Tris base (cat. 10708976001, Sigma-Aldrich), NaCl (S6191, Sigma-Aldrich), and proteinase K (cat. EO0491, Thermo Fisher Scientific). Finally, the gel was expanded by immersion in 15 mL of double-distilled H_2O three times for 1 h each time (gel expansion reached a plateau after the original 12 mm gel diameter expanded to ∼50 mm). Samples were transferred to a 35 mm diameter glass-bottom Petri dish (cat. 81218-200, ibidi) coated with 600 μL of poly-L-lysine (cat. P4707, Sigma-Aldrich) and incubated for 15 min at room temperature. Images were acquired using an LSM880 laser scanning confocal microscope (Carl Zeiss AG) and a 63× oil objective (numerical aperture, NA 1.2).

Table 2. Composition of Denaturation Buffer

component	concentration[a]
Triton X-100	0.5 g
ethylenediaminetetraacetic acid	0.027 g
Tris (1 M) aqueous solution, pH 8	5 mL
NaCl	4.67 g
proteinase K	800 units

[a]Final concentration (per 100 mL solution).

Data Processing and Analysis. Immunofluorescence images for image analysis were captured by confocal microscopy with a super-resolution Airyscan detector (LSM880, Carl Zeiss AG) and with an Elyra 7 structured illumination microscope equipped with a super-

https://doi.org/10.1021/acsbiomaterials.2c00650
ACS Biomater. Sci. Eng. 2022, 8, 4789−4806

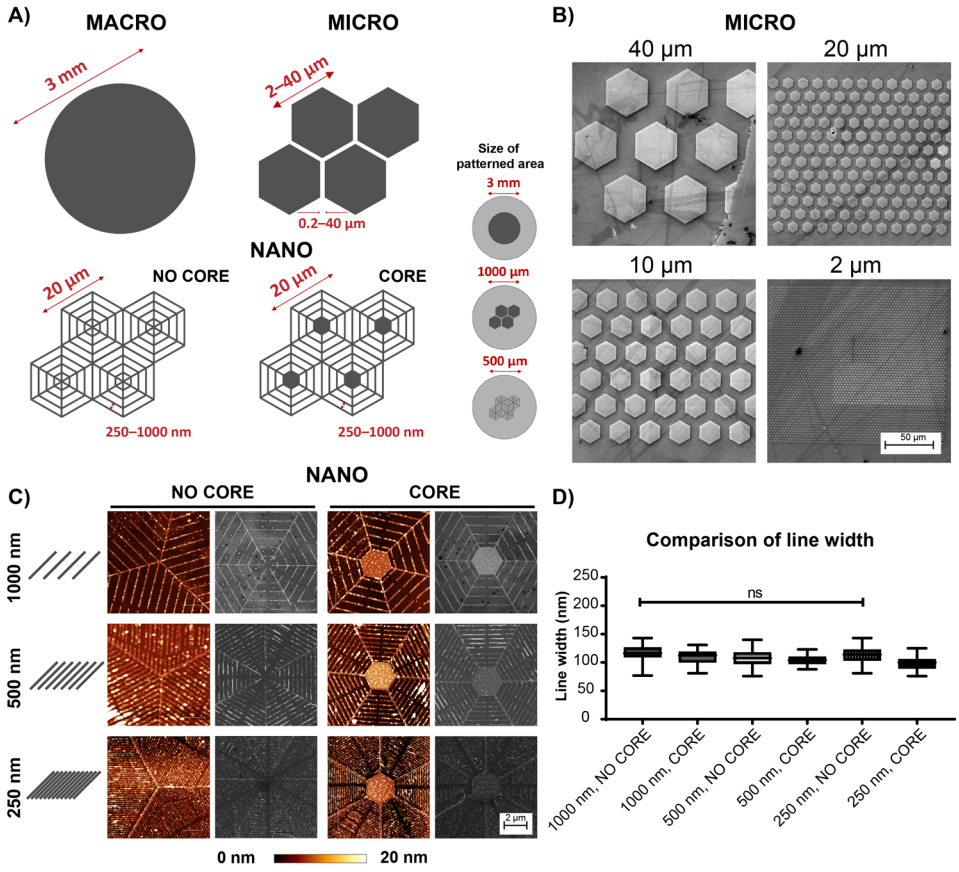

Figure 2. Electron-beam lithography allows the production of precise structures with a variety of MICRO and NANO distributions. (A) Schematic of designed surfaces used in the study: circular MACRO surfaces with diameters of 3 mm, hexagonal MICRO patterns that were differently distributed with increasing size (2−40 μm), and NANO hexagonal structures with diameters of 20 μm with a variety of line distributions. NO CORE and CORE variants represent hexagons without and with filled hexagonal centers, respectively. The total sizes of the patterned areas of the structures are listed on the right side of the graphic (MACRO = 3 mm, MICRO = 1000 μm, and NANO = 500 μm). (B) SEM characterization of MICRO hexagons of different diameters, as prepared by EBL. Scale bar = 50 μm. (C) AFM and SEM topography of prepared hexagonal nanopatterns with spacings of 1000, 500, and 250 nm in NO CORE and CORE variants. Scale bar = 2 μm. Error bars represent ± standard error of the mean. (D) Line widths for each variant were measured on cross-sections of AFM images (n = 50 cross-sections) and were estimated by the full width at half-maximum. The average line width was close to 100 nm. Image analyses were performed in ImageJ Fiji and with software from JPK Instruments. The statistical analyses were performed using an unpaired t test. ns, not significant.

resolution structured illumination microscopy (SIM) module. The number of ephrin A ligand clusters were analyzed using Fiji (https://imagej.net/software/fiji/) and Imaris (RRID:SCR_007370) software used for voxel analysis.[69] Statistical analyses were performed using independent-sample t tests in GraphPad Prism version 9.0.0 for Windows (GraphPad Software, San Diego, CA, www.graphpad.com).

RESULTS AND DISCUSSION

Deposition of 100 nm Wide Hexagonal Nanopatterns on a Cover Glass Substrate Using a Modified Electron-Beam Lithography Workflow. EBL allows for a very precise spatial nanodistribution of biomolecules. Field stitching can distribute a nanopattern over a relatively large surface area.[70] Thus, we decided to use this approach to develop our model system. We initiated our experiments with a conventional EBL workflow for depositing grid-lines (Figure 1A).[71] Briefly, an electron-sensitive resist layer is usually spin-coated onto the substrate surface, and the electron beam creates the nanopattern in this resist layer. The entire surface is then sputter-coated with platinum (or an alternative material) from which the final pattern is made. During the last step (called "lift-off"), the areas of the resist layer that were not exposed to the electron beam are washed out, so that only the pattern in the form of deposited material remains on the surface. However, several of these steps had to be altered in our experimental setup to ensure the compatibility of EBL with a cell-culture-compatible substrate, specific binding of proteins to the deposited nanopatterns, and stable cohesion of complex hexagonal nanopatterns on the surface.

First, we included a layer of ITO to ensure the compatibility of EBL with our chosen substrate—quartz-based cover glasses used for cell culture. Standard EBL protocols are usually performed on a special substrate (e.g., a silicon wafer) that has good electron-conducting properties necessary to prevent charging distortion.[70,72,73] However, a quartz-based substrate has poor conductive properties, which leads to the deflection of incoming electrons by surface charges and is a significant source of pattern-placement error. Therefore, to eliminate this drifting effect, a thin layer (20 nm) of ITO was sputter-coated onto the cover glass substrate to ensure electron-conductive properties.[74,75] This deposition successfully eliminated beam drifting on a sample surface coated with ITO and allowed the production of precise patterns of grid-lines of approximately 100 nm in width (Figure 1B), a resolution comparable to the

https://doi.org/10.1021/acsbiomaterials.2c00650
ACS Biomater. Sci. Eng. 2022, 8, 4789−4806

EBL limits obtained with standard silicon-wafer surfaces.[41] Importantly, it also allowed us to prepare complex hexagonally distributed patterns that can be assembled to create larger patterns that better reflect the geometrically circular organization of eukaryotic cells.

Second, we implemented a PEG coating in our protocol to enhance the specificity of biomolecule binding to the nanostructure pattern. NSA of biomolecules affects the sensitivity, reproducibility, and cell-interaction specificity of many cell-interaction studies.[49,50,76] Indeed, we found that our selected HaloTag-fused biomolecule was nonspecifically adsorbed to ITO-coated surfaces. To avoid this adverse effect, we tested an array of 97 PEG solutions: a panel of 96 commercially available PEG solutions (NeXtal Tubes PEGs Suite, NeXtal) and an additional poly-L-lysine-g-polyethylene glycol (PLL-g-PEG) solution supplied by SuSoS Surface Technology (Table S1). ITO-coated surfaces for EBL were incubated with the 97 PEG solutions and then with a select HaloTag-fused biomolecule. To evaluate the level of NSA of proteins to ITO surfaces, the adsorbed biomolecule was fluorescently stained with an antibody against the HaloTag. Subsequently, the fluorescence intensity of the nontreated ITO surface and the ITO surface treated with different PEG solutions was measured and compared. The data showed that 10 of the 97 PEGs successfully eliminated NSA. However, after further application of an electron-sensitive resist layer and surface dehydration by heating to a high temperature (150 °C), most PEG variants underwent thermal degradation, as described previously.[77] Thus, only three candidates (PEG-10, PEG-15, and PLL-g-PEG) preserved the protein-repulsive characteristic after layering. As shown in Figure 1C, PEG-10 and PEG-15 reduced protein NSA to the surface by 50% compared with ITO surfaces without PEG coating (NO PEG). As the PLL-g-PEG reduced NSA to the greatest extent (~98%), we used this molecule in all subsequent EBL-manufacturing procedures.

Third, we utilized the proadhesive tantalum layer to ensure the firm adhesion of EBL-deposited material. The addition of this step was prompted by the observation that the nanolines peeled off randomly from the surface, especially in cases when the EBL procedure was used to prepare high-density hexagonal nanopatterns in combination with PEG layering (Figure 1D, +PEG/−tantalum). We hypothesized that this effect was caused by low cohesion of sputtered material (platinum) to the surface, because of the protein-repulsive layer of PEG, or a high density of lines that complicated accessibility of the lift-off solution, NEP, to the electron-sensitive layer. Thus, we first increased the adhesivity of the nanolines by using a thin tantalum layer, previously reported to have proadhesive properties.[78] These modifications led to the successful deposition of hexagonal nanopatterns (Figure 1D, +PEG/+tantalum). The quality of nanopatterns created by conventional (−PEG/−tantalum) and modified (+PEG/+tantalum) EBL protocols was compared by measuring the line width on more than 50 cross-sections from each surface using atomic force microscopy (AFM). Moreover, our data confirmed that adding ITO, PEG, and tantalum had no adverse effect on line width (Figure 1E).

We also modified the design of the hexagonal nanopatterns by implementing a 300 nm interruption into the nanohexagonal design (Figure 2C) to increase the accessibility of NEP and ease lift-off. This modification led to more consistent production of nanopatterns (data not shown). Thus, taken together, our initial optimization of the EBL procedure allowed us to successfully deposit a 100 nm wide hexagonally distributed pattern on cell culture (cover glass) substrates with high resolution and comparable width to standard EBL on silicon wafers.

Electron-Beam Lithography Allows the Production of Precise Structures in Microscale and Nanoscale Distributions. To demonstrate the potential and scalability of this technique, we designed a panel of MICRO and NANO surfaces with different structure densities to obtain diverse conditions for studying and modulating cellular interactions. We also prepared a control MACRO surface by sputter-coating through a polydimethylsiloxane stencil mask (Alvéole). As presented in Figure 2A, we created circular MACRO surfaces (3 mm diameter), hexagonal MICRO patterns of increasing size (2−40 μm) and distribution (0.2−40 μm) (scanning electron microscopy [SEM] characterization in Figure 2B), and NANO hexagonal structures of 20 μm diameter with different line distributions. We successfully reached line spacings of 1000, 500, and 250 nm (Figure 2C), which correspond to the cell membrane distribution of many ligands and receptor classes, including glycosylphosphatidylinositol-anchored ephrin A ligands.[79] We also created two NANO surfaces at each line density without (NO CORE) and with (CORE) a hexagon-shaped filled center 2 μm in diameter, with the assumption that hexagonal patterns with filled centers would enhance cell adhesion.

We subsequently defined specific parameters of EBL for different line densities within the NANO pattern. The electron dose (μC cm^{-2}) influences both the width and spacing of lines produced during EBL. The lower the dose, the thinner the structure and the higher the line density. A lower electron dose allows faster preparation of denser (250 nm) nanohexagons, which reduces the procedure's cost and increases its effectiveness, especially when covering large, cell-culture-relevant surface areas (e.g., 500 × 500 μm). Thus, to obtain 100 nm wide structures with line spacings of 1000, 500, and 250 nm, we optimized the beam dosage to 92 μC cm^{-2} for 1000 nm, 88 μC cm^{-2} for 500 nm, and 86 μC cm^{-2} for 250 nm (data not shown). The line resolution for each variant was subsequently validated by detailed AFM topography measurements, which confirmed line widths close to 100 nm (Figure 2D). Notably, there was no significant difference between the line width obtained on differently distributed nanohexagonal patterns (Figure 2D). Thus, by using our optimized parameters, we shortened the time to produce hexagonal nanopatterns over an area sufficient for cell culture (500 × 500 μm) to 1 h.

The EphA2 Biomolecule Immobilized via the HaloTag System Shows Specific Binding to Hexagonal Nanostructures Created by Electron-Beam Lithography. We used the HaloTag system to immobilize our selected protein, EphA2, onto our patterned surfaces with optimized EBL technology. As a proof of concept biomolecule, we chose EphA2 because it regulates morphological processes, including tissue patterning and spatial-temporal cell positioning during development.[80−82] Additionally, increasing evidence suggests that the Eph receptor/ephrin protein family is susceptible to a nanodistribution of molecules within the cell membrane, making this molecule an ideal candidate for our studies.[61,83] EphA2 has more than one type of ephrin A ligand; therefore, its multiple binding partners can be analyzed by surface immobilization of EphA2.[84−86] Importantly, our preliminary

https://doi.org/10.1021/acsbiomaterials.2c00650
ACS Biomater. Sci. Eng. 2022, 8, 4789−4806

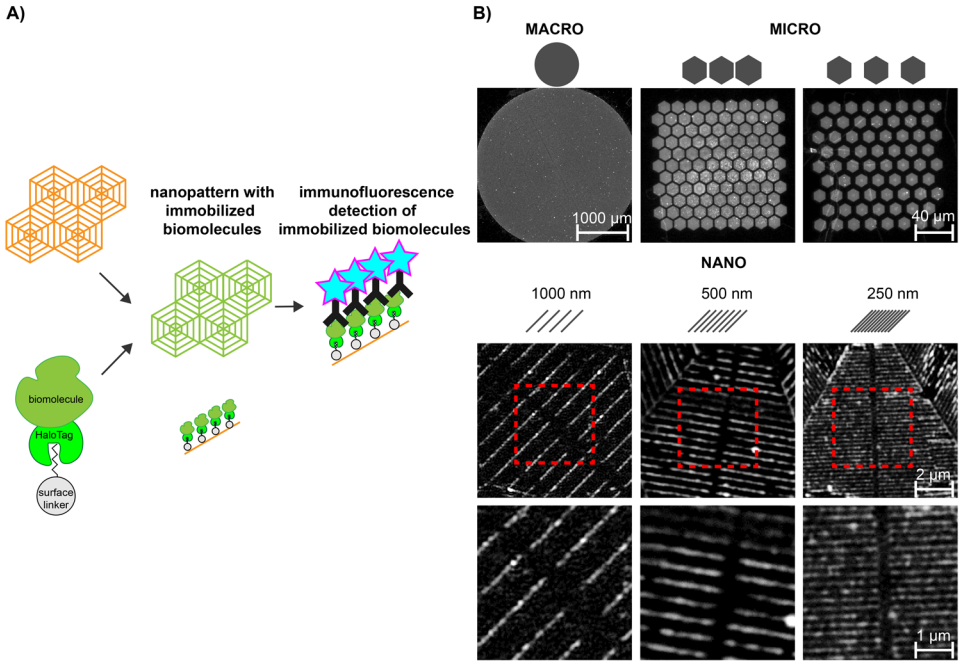

Figure 3. Visualization of EphA2 biomolecules immobilized via the HaloTag system on hexagonal nanostructures created by electron-beam lithography. (A) Schematic illustration of HT-EphA2 immobilization via a surface linker and its subsequent immunolabeling with a primary antibody against HaloTag and a secondary antibody conjugated with a fluorophore (alexaFLuor-488). (B) Upper panel: confocal immunofluorescence microscopy images of MACRO (platinum circle) and MICRO patterned surfaces. Lower panel: super-resolution SIM of NANO patterns (1000, 500, and 250) showing a high specificity of L-HT-EphA2 binding toward structures on various levels. Scale bars are depicted in each image: 1000 μm for MACRO, 40 μm for MICRO, and 2 and 1 μm for nanopatterns.

quantitative PCR analysis showed that, out of 22 known Eph receptor/ephrin family members, our model cell type, hPSCs, expressed several Eph receptor genes, including *EPHA2*, as well as ephrin ligands, confirming the presence of this signaling pathway in hPSCs (Figure S1A).[87] Further experiments verified the presence of the EphA2 receptor and its five ligands (i.e., ephrin A1, A2, A3, A4, and A5, Figure S1B,C) by immunofluorescence and Western blot, with ephrin A4 having the lowest expression.

We immobilized the EphA2 receptor on nanopatterned platinum, as shown in Figure 3A, by using a fusion protein consisting of EphA2 and HaloTag (HT-EphA2). Covalent immobilization of recombinant HT-EphA2 at the nanoscale was then achieved via a thiol linker. We confirmed specific binding of the thiol linker to the relevant epitope of the HT-EphA2 protein complex by MALDI-TOF analysis. Successful formation of this covalent bond (linker-HT-EphA2; L-HT-EphA2) is represented by an intensity peak shift in mass-to-charge ratio (m/z) from 92 226 to 92 760 (Figure S2). Thus, our results are in line with other studies that showed the suitability of the HaloTag tethering method for site-specific covalent immobilization of proteins to a variety of metal and nonmetal surfaces with high binding stability.[54,88]

Lastly, to confirm the specificity of L-HT-EphA2 immobilization, we performed immunofluorescence detection of L-HT-EphA2 binding to patterns represented as MACRO (3 mm diameter circles), MICRO (2−40 μm diameter hexagons), and NANO (20 μm diameter hexagons). Immunolabeling revealed high binding specificity of the protein complex to metal structures with a high signal-to-noise ratio. As shown in Figure 3B, microscopy images of MACRO, MICRO, and NANO patterned surfaces confirmed a high specificity of L-HT-EphA2 binding toward the structures at all levels, including the most challenging nanopattern that we tested (100 nm lines with 250 nm spacing). These data demonstrate that the two-step immobilization process is highly specific, effective, and comparable with the currently used, one-step dip-pen lithography technique.[89,90]

EphA2 Immobilized to Macroscale and Microscale Surfaces Supports Human Pluripotent Stem Cell Adhesion and Spreading. Upon successfully combining EBL and immobilization procedures, we proceeded to experiment with our selected cellular model, hPSCs. In contrast to the immortalized cancer cell line MDA-MB-231, the most commonly used in such Eph receptor/ephrin localization studies, hPSCs are extremely sensitive to the composition and nature of their surrounding environment.[58,91,92] Thus, they represent a valuable model for cell-surface interaction studies as their ability or inability to adhere to the cell culture substrate clearly defines the robustness of the designed microenvironment. Further, their pluripotency makes them a worthy candidate to study the effect of single-molecule nanodistributions on cellular differentiation in the future.

First, we analyzed the interaction of hPSCs with MACRO-distributed L-HT-EphA2. As it was previously shown that biological cues are highly affected by topographical and biochemical changes of biomaterials, we experimentally determined the optimal L-HT-EphA2 concentration to be 5 μg mL^{-1} (Figure S3A,B).[93] It is also known that this family of tyrosine kinase proteins influences the actin cytoskeleton, affecting cell shape and adhesion.[94] Thus, we evaluated morphology, cell adhesion and spreading as a response to microenvironmental cues as an experimental readout. Our results show that hPSCs specifically interact with L-HT-EphA2 proteins covalently immobilized to the platinum MACRO surface (Pt+L-HT-EphA2; Figure 4A). No cellular interactions

https://doi.org/10.1021/acsbiomaterials.2c00650
ACS Biomater. Sci. Eng. 2022, 8, 4789−4806

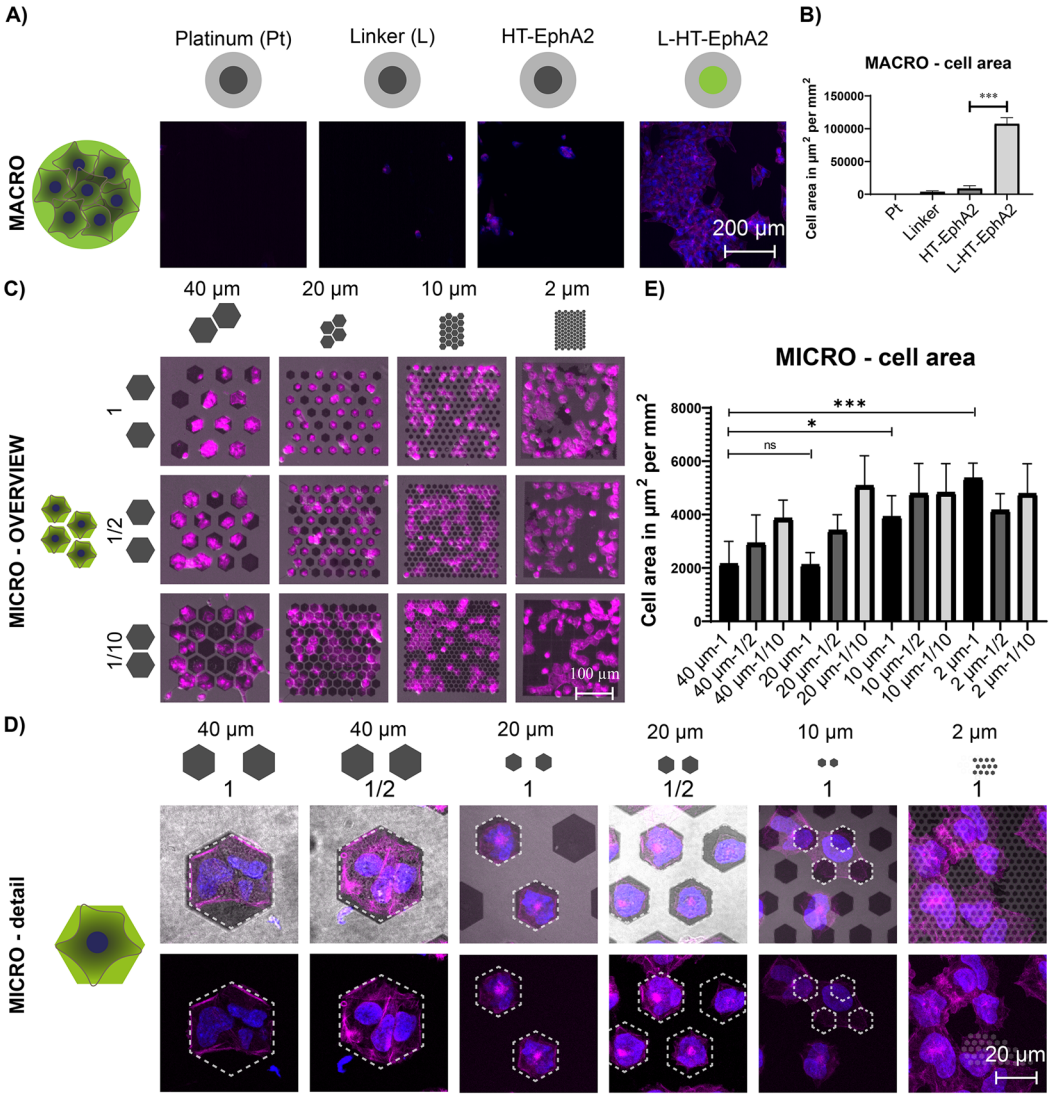

Figure 4. EphA2 immobilized to MACRO and MICRO surfaces supports human pluripotent stem cell adhesion and spreading. (A) Wide-field fluorescence microscopy (cytoskeleton = magenta; nucleus = blue) of cell interactions with L-HT-EphA2 protein covalently immobilized to the platinum MACRO surface (Pt+L-HT-EphA2). No cellular interactions were observed on the control surfaces without EphA2 protein (Pt and Pt +linker), and only a few cells were attached to the surfaces with immobilized biomolecules without linker (Pt+EphA2-HT), likely because of interference by residually adsorbed proteins. Scale bar = 200 μm. (B) Image analysis of cell spreading on MACRO surfaces with immobilized HT-EphA2 and controls. Error bars represent ±standard error of the mean (n = 4). (C) Wide-field fluorescence microscopy (cytoskeleton = magenta) showing interaction with covalently immobilized HT-EphA2 at the MICRO level and with variation in the gaps between hexagons as measured by pattern diameter (1, 1/2, and 1/10 pattern diameter). Cell interactions are influenced by the diameter of different MICRO hexagons (40, 20, 10, and 2 μm). Scale bar = 100 μm. (D) Detailed images obtained from laser scanning confocal microscopy illustrating cells spreading on a variety of MICRO diameters and distributions. Scale bar = 20 μm. (E) Image analysis of cell spreading on MICRO surfaces with L-HT-EphA2 and different pattern distributions. Error bars represent ± standard error of the mean (n = 9). Image analyses were performed in ImageJ Fiji. The statistical analyses were performed using an unpaired t test. *p < 0.1 and ***p < 0.001. ns, not significant.

were observed on the surfaces without EphA2 protein (Pt and Pt+linker), and only a few cells attached to the surfaces with immobilized biomolecules without the linker (Pt+HT-EphA2), likely because of interference by residually adsorbed proteins. Cell attachment was quantified using image analysis of cell spreading (Figure 4B), and we confirmed that hPSCs attached significantly and specifically only to the platinum surface with immobilized L-HT-EphA2. Thus, we confirmed that immobilized EphA2 biomolecules initiate cell attachment. Interestingly, our model system, based on immobilization of the Eph receptor, contrasts with most current experimental setups that focus on the Eph receptor/ephrin signaling system. The other experiments mostly examine the influence of immobilized ephrin ligands on activation of Eph receptors by measuring their level of kinase-domain phosphorylation.[95]

Next, we created MICRO surfaces with immobilized L-HT-EphA2 proteins to test whether cells could specifically attach and respond to the microdistribution of L-HT-EphA2. As described above, we prepared hexagonal micropatterns with different hexagon diameters and spacings between hexagons (Figure 2A, B). Selected hexagon diameters (40, 20, 10, and 2 μm) were chosen to be biologically relevant to the diameter of hPSCs.[96] The sizes of the gaps between hexagons were selected to test different conditions for cell interactions and

https://doi.org/10.1021/acsbiomaterials.2c00650
ACS Biomater. Sci. Eng. 2022, 8, 4789−4806

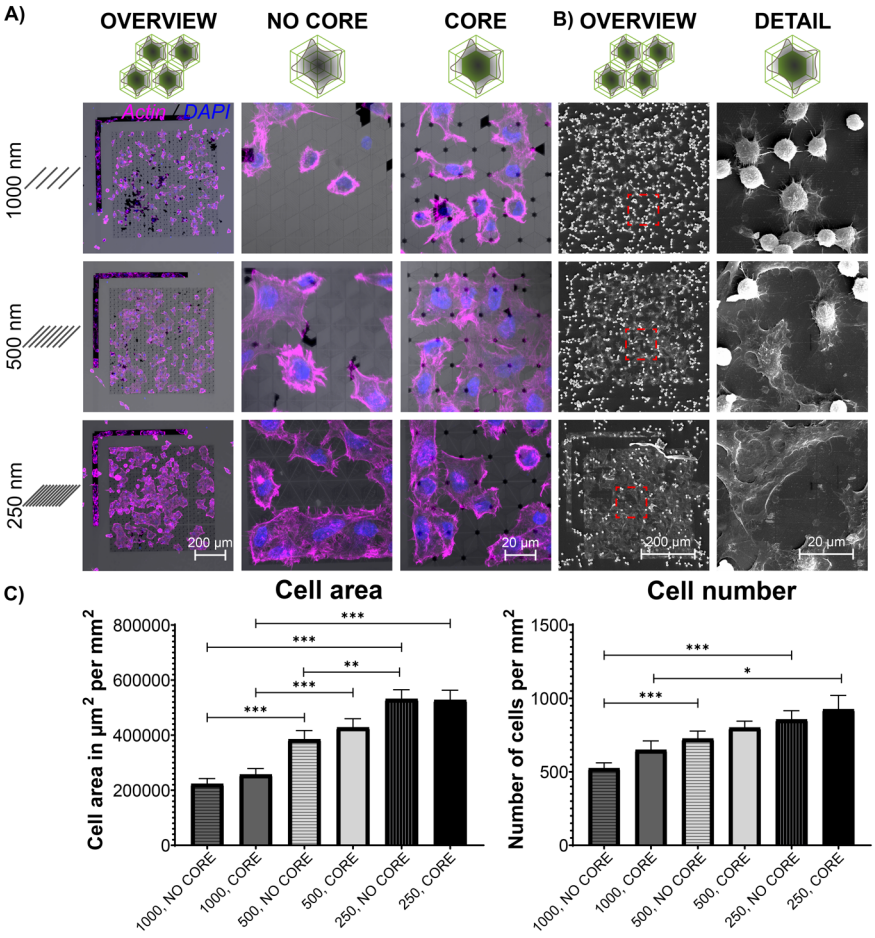

Figure 5. Differences in the nanodistribution of EphA2 caused variations in human pluripotent stem cell adhesion and spreading. (A) Left panel: overview of laser scanning microscopy (cytoskeleton = magenta; nucleus = blue) combined with bright-field microscopy (visualizing the nanostructures) showing specific cell interactions with nanodistributed regions. Middle and right panels: images of the NO CORE and CORE variants showing differences in cell spreading and cell morphology obtained on differently nanodistributed L-HT-EphA2 (line spacings of 1000, 500, and 250 nm). (B) Overview of specificity of cell interactions by SEM, and images depicting the high-resolution differences in morphology of cell interactions on differently nanodistributed L-HT-EphA2 (line spacings of 1000, 500, and 250 nm). (C) Image analyses of cell number and cell area on different nanopatterned areas, obtained from wide-field fluorescence microscopy. Scale bar = 20 μm. All error bars represent ±standard error of the mean (n = 9). Image analyses were performed in ImageJ Fiji. The statistical analyses were performed using an unpaired t test. *p < 0.1, **p < 0.01, and ***p < 0.001.

were spaced in accordance with the hexagon diameter. Therefore, the gaps between hexagons were labeled as "1 pattern diameter", "1/2 pattern diameter", and "1/10 pattern diameter". The adhesion of hPSCs was evaluated 4 h after plating, a time sufficient for cell spreading and establishing cell−surface interactions.[97,98] As shown in Figure 4C, cells specifically attached to the microdomains of immobilized L-HT-EphA2 and adapted their cytoarchitecture toward the pattern geometry. As shown in Figure 4D in greater detail, the 40 μm domains were occupied by several cells, whereas the 20 μm domains were mostly occupied by only one cell, likely due to the increased size of spreading hPSCs. Notably, decreasing the gap size between the patterns tended to allow more cells to spread on two micropatterns simultaneously. On micropatterns with hexagon diameters smaller than 20 μm and distances between hexagons of 1/2 pattern diameter, cells almost invariably spanned the space between separated hexagons and interacted with the surrounding hexagons. These results indicate that a distance between patterns that is smaller than the diameter of a spreading cell is crucial for cells to bypass gaps; the 1/2 pattern diameter (for diameters 2−10 μm) and 1/10 pattern diameter (for all diameters) allowed cells to migrate and spread. Each cell stayed individually on those patterns on the more separated hexagons. These observations were also confirmed using image analysis of cell spreading (Figure 4E). Taken together, we affirmed that a restricted spatial distribution of biomolecules drives cells to adapt their cytoskeletons toward the patterned shape. Cytoskeletal analysis of actin filaments (Figure 4E) confirmed that hPSCs also perceive changes in biomolecule distribution at the microscale and that they specifically respond to this microdistribution. Moreover, we show that hPSCs can interact with biomolecules at the microscale. These results are consistent with previous cell−ECM studies on microdistributed integrin adhesive proteins and on a cell model of human mesenchymal stem cells.[99,100]

A Specific Nanodistribution of EphA2 Induces Specific Adhesion and Spreading of Human Pluripotent Stem Cells. Upon verifying that MACRO and MICRO surfaces coated with EphA2 receptors facilitate the attachment of hPSCs, we evaluated whether selected NANO patterns also supported the adhesion and spreading of hPSCs, as these cells

https://doi.org/10.1021/acsbiomaterials.2c00650
ACS Biomater. Sci. Eng. 2022, 8, 4789−4806

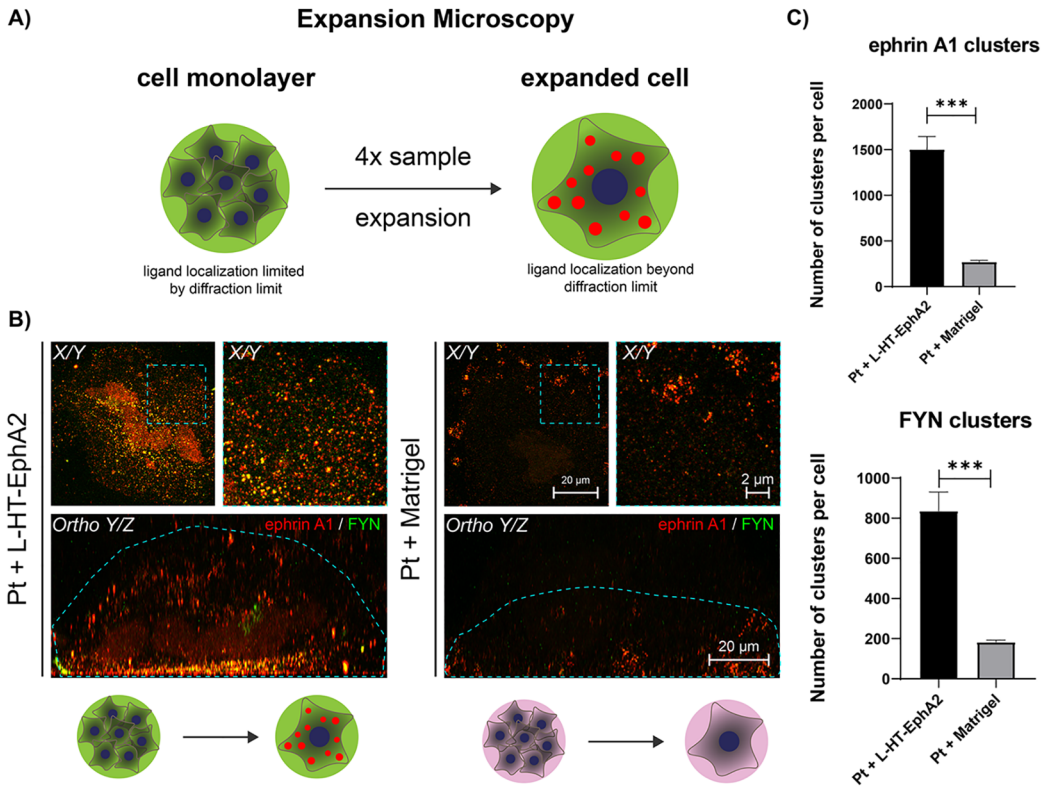

Figure 6. Human pluripotent stem cells organize membrane-bound ephrin A1 ligand toward macrodistributed L-HT-EphA2. (A) Illustration of ExM sample preparation to overcome the spatial-diffraction resolution limit. Ligand organization within the cell membrane is hidden in the nonexpanded sample and revealed by expansion of the samples. (B) Confocal fluorescence microscopy images of an expanded cell on surfaces coated with L-HT-EphA2 or Matrigel. Images were obtained by orthogonal projection of multiple *Z*-stacks of one cell. The orthogonal projection on *X*/*Y* shows that the ephrin A1 and FYN cluster colocalize in a single cell. The orthogonal projection Ortho *Y*/*Z* shows ephrin A1 (red) localization toward the immobilized L-HT-EphA2 protein. A greatly lower signal from this clustering appeared on the Matrigel surface, and the ephrin A1/FYN signal was localized toward the periphery of the cell membrane. Scale bar = 2 or 20 μm. (C) Quantification of the number of ephrin A1 and FYN clusters per cell detected on immobilized L-HT-EphA2 or Matrigel. All error bars represent ±standard error of the mean (n = 3). Image analysis was performed in ImageJ Fiji. The statistical analyses were performed using an unpaired t test. ***$p < 0.001$.

have a very narrow area for interactions. There is evidence that many cell types respond specifically to the nanodistribution of biomolecules; however, to date, there has been no reported evidence that hPSCs can specifically attach to such nanopatterned surfaces.[101−103] Therefore, we used our optimized concentric hexagonal nanopatterns with (CORE) or without (NO CORE) filled centers combined with a covalently attached L-HT-EphA2 biomolecule. As shown in Figure 5A, laser scanning confocal microscopy (visualizing the cytoskeleton and nuclei) combined with bright-field microscopy (visualizing the nanostructures) confirmed direct cell interaction with the nanopatterned region. Specifically, hPSCs attached to L-HT-EphA2 with lines spaced at 1000, 500, and 250 nm but did not attach to the nonpatterned surrounding surface. Thus, we reveal a specific interaction of hPSCs with nanopositioned EphA2 ligands.

However, a detailed image analysis of the tested variants revealed differences in cell spreading and cell morphology on differently nanopatterned L-HT-EphA2 (line spacings of 1000, 500, and 250 nm). As shown in Figure 5A, fluorescence analysis of the distribution of the cell cytoskeleton revealed nanopattern density-dependent cell spreading, with the highest spreading at a pattern density of 250 nm and the lowest spreading at a pattern density of 1000 nm. Additionally, SEM analysis complemented these results and clearly showed that the increasing pattern density significantly improved the spreading of hPSCs on nanopatterned surfaces (Figure 5B). Quantification of cell number and cell area covered in each condition confirmed these observations. As shown in Figure 5C, significantly more cells were attached to or spread over 250 nm patterns and 500 nm patterns than for 1000 nm patterns. Moreover, although not statistically significant, quantitative image analysis revealed a trend toward higher cell numbers and better cell spreading with CORE patterns compared with NO CORE patterns (Figure 5C). These results confirmed that hPSCs are highly susceptible to nanodistributed EphA2 biomolecules within their environment, demonstrating that our system is useful to control and study cell interactions at a single-cell level.

Human Pluripotent Stem Cells Organize Membrane-Bound Ephrin A1 Ligand toward Immobilized L-HT-EphA2. Our experimental system confirmed that the combination of optimized EBL technology with covalently bound HaloTag-fused biomolecules effectively supports cell interaction, adhesion, and spreading of hPSCs on large-scale MACRO, MICRO, and narrow NANO surfaces. However, it was unknown whether this interaction was ephrin ligand-specific and could be used for single-molecule studies. Thus, we investigated whether immobilized EphA2 receptors could be exploited to determine the localization and behavior of its

https://doi.org/10.1021/acsbiomaterials.2c00650
ACS Biomater. Sci. Eng. 2022, 8, 4789−4806

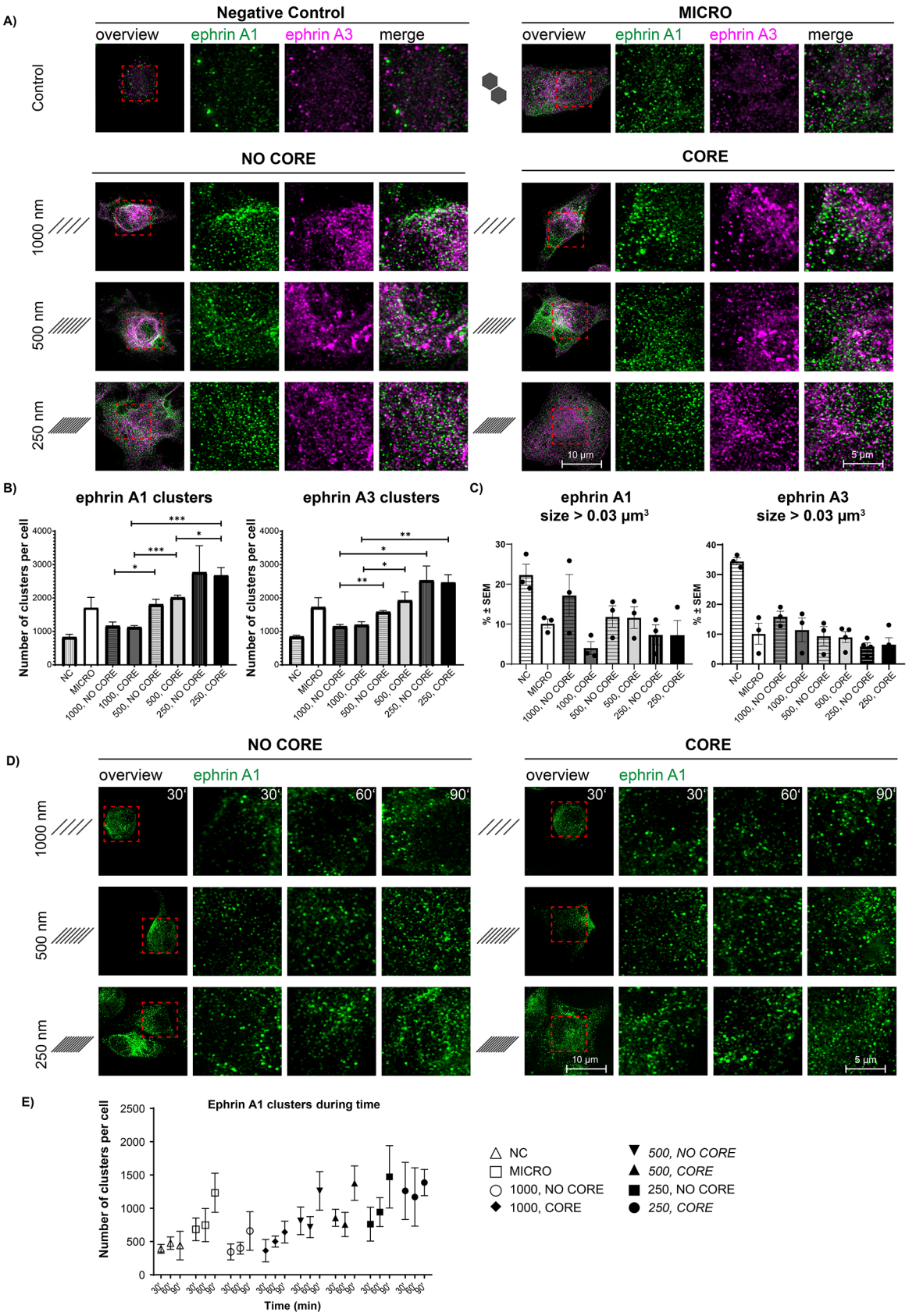

Figure 7. Nanopatterned EphA2 influences intracellular localization, clustering, and dynamics of ephrin A ligands of human pluripotent stem cells. (A) Maximum intensity projection of super-resolution SIM of ephrin A1 (green) and ephrin A3 (purple) ligands. The images in the first column are an overview of the entire single cell attached to the surface. The red square represents an area that was cropped and zoomed, which is shown to better visualize cluster formation. Images show differences in the formation of ligand clusters at different nanodistributions (line spacings of 1000, 500, and 250 nm) and on hexagons with empty cores (NO CORE) or with filled cores (CORE). Negative control (nonstructured surface without

https://doi.org/10.1021/acsbiomaterials.2c00650
ACS Biomater. Sci. Eng. 2022, 8, 4789−4806

Figure 7. continued

L-HT-EphA2) and positive control MICRO (with immobilized L-HT-EphA2) surfaces are also depicted, showing the level of cluster formation without nanopatterns. Scale bars = 10 and 5 μm. (B) Quantification of the number of ephrin A1 and ephrin A3 clusters for all experimental surfaces. (C) Quantification of the percentage of larger clusters of ephrin A1 and ephrin A3 clusters for all experimental surfaces. Error bars represent ±standard error of the mean (n = 3 for volume analysis, n = 3 for cluster-number analysis). (D) Super-resolution SIM characterization of ephrin A1 cluster-formation dynamics on nanopatterned L-HT-EphA2. Maximum intensity projection of SIM of ephrin A1 ligand (green) distribution within hPSCs fixed at three different time points (30, 60, and 90 min) on different surfaces (line spacings of 1000, 500, and 250 nm) and on hexagons with empty cores (NO CORE) or with filled cores (CORE). The images in the left columns of each set (NO CORE and CORE) are an overview of the entire single cell attached to the surface at 30 min. The red square represents an area that was cropped and zoomed, which is shown for better visualization of cluster formation. Scale bars = 10 and 5 μm. (E) Quantification of the number of ephrin A1 clusters per cell at several time points. Error bars represent ±standard error of the mean (n = 10). Image analyses were performed in Imaris and ImageJ Fiji. The statistical analyses were performed using an unpaired t-test. *p < 0.1, **p < 0.01, and ***p < 0.001.

ligands and possibly also their activation. We first selected ephrin A1, the main EphA2-binding partner, as a proof of concept molecule for these studies.[104−107] However, as Eph receptor/ephrin forms clusters at subdiffraction-limited sizes that are highly dynamic and temporary, the evaluation of the distribution and activity of these ligands is nontrivial.[108] To overcome this technical challenge, we used expansion microscopy (ExM), which enables high-resolution imaging in the entire volume of individual cells (Figure 6A), and performed coimmunostaining of ephrin A1 with FYN kinase, an intracellular ephrin A1 downstream signaling molecule that, upon activation of the EphA receptor/ephrin A signaling pathway, regulates the ephrin A ligand membrane distribution and thus cell adhesion.[109−113]

In our experiments, receptor and ligand interaction was evaluated by comparison of cells attached to a MACRO surface with immobilized EphA2 and by cells plated on a standard cell culture surface (Matrigel-coated) 4 h after plating. Specific cell membrane sequestration of ephrin A1 ligands and FYN kinase toward the platinum surface with immobilized L-HT-EphA2 was observed (Pt+L-HT-EphA2; Figure 6B). Furthermore, the merged signal confirmed a high level of ephrin A1 and FYN colocalization, confirming active Eph receptor/ephrin A1 signaling. In contrast, only a weak signal was emitted by cells seeded on the control substrate, Matrigel (Pt+Matrigel), and the signal was localized mainly at the cell periphery, where cells usually form focal adhesion sites. Quantification of ephrin A1 and FYN clusters formed for each condition is shown in Figure 6C and confirms significantly upregulated numbers of clusters on the cell surface with immobilized EphA2 receptors. Our results clearly show that cells seeded on the L-HT-EphA2 surface actively interacted with this surface via the ephrin A1 ligand. They also prove that the surface distribution of biomolecules induces a specific cell response; in our case, we observed a higher distribution of ephrin A1 ligand toward the surface and higher activation of ephrin A1 ligand.

Nanopatterned EphA2 Influences Intracellular Localization, Clustering, And Dynamics of the Ephrin A Ligands in Human Pluripotent Stem Cells. We tested whether the intracellular localization, clustering, and dynamics of the ephrin A ligands are influenced by the nanodistribution of the L-HT-EphA2 receptor. The effect of nanodistribution on cluster formation of integrin has been previously shown.[114] Out of all of the ephrin A ligands that we tested, we found that ephrins A1, A2, A3, and A5 are distributed within hPSCs, and ephrins A1 and A3 show the most prominent nanopattern-induced clustering. Thus, we performed super-resolution SIM to compare the number and size of ephrin A1 and A3 clusters. As shown in Figure 7A, all analyzed nanopatterns supported the formation of ephrin ligand clusters. In particular, ephrin ligand clusters varied in their number and size with respect to different hexagonal nanodistributions (line spacings of 1000, 500, and 250 nm) and were markedly larger on low-density nanopatterns. Specifically, our data show that low-density nanopatterns (1000 nm) resulted in a lower number of larger ligand clusters. In contrast, high-density nanopatterns (250 nm) resulted in a higher number of smaller ligand clusters (Figure 7B, C). Control micropatterned surfaces (with immobilized L-HT-EphA2) and nonpatterned surfaces (without the biomolecule; negative control) are also illustrated. The same concentration of biomolecules was applied to MICRO and NANO hexagons with a diameter of 20 μm. Although the density of immobilized biomolecules is the same for both, for NANO patterns it is arranged in 100 nm lines that are spaced apart, so that the number of molecules per area decreases with 250, 500, and 1000 nm spacing. Accordingly, a correlation between the number of ephrin A clusters formed and the density of immobilized molecules was expected. If the dependence was directly proportional to the number of molecules per area, the highest number of clusters should be for MICRO hexagons. The lowest number of clusters was formed on the 1000 nm pitch hexagons; as expected, a medium number was formed on the 500 nm pitch hexagons, which was comparable to the number of clusters formed on the MICRO hexagons. The highest cluster formation was then induced on 250 nm pitch hexagons. Together these findings indicate that not only the amount but also the nanodistribution of biomolecules influences cell response to immobilized molecules. A similar effect of EphA2 nanodistribution was observed on the number of ephrin A2 and A5 clusters but not on their size (Figure S4A−C), likely because these ligands have a stronger affinity toward the EphA3 receptor.[115] Finally, a comparison of NO CORE and CORE variants of nanohexagonal structures does not reveal significant differences between the number of formed ephrin A clusters. The primary intent of the nanopatterned CORE variant was to centrally initiate cell adhesion and spreading. The area of added centers in this variant covers 3 μm^2 in comparison to 300 μm^2 of the whole nanohexagon. Within 60 min after cell seeding, cells preferentially attached to the CORE variant compared to NO CORE variants; however, after 4 h, when ephrin clusters were analyzed, most of the cell space was primarily affected by nanodistributed lines in the hexagonal patterns. Minimal differences were thus observed between NO CORE and CORE variants of nanohexagonal structures.

Additionally, we investigated whether cluster formation dynamically changes over time and with changes in nanodistribution pattern density. It was previously shown that EphA

https://doi.org/10.1021/acsbiomaterials.2c00650
ACS Biomater. Sci. Eng. 2022, 8, 4789−4806

receptor/ephrin A membrane clustering and internalization is a fast, dynamic process that occurs within 10−15 min to several hours after cell seeding.[95] Thus, to evaluate this dynamic process, we seeded the cells on all experimental surfaces and subsequently fixed them at three different early time points: 30, 60, and 90 min. We show that the specific nanodistribution of the EphA2 receptor affects the clustering dynamics of the membrane-associated ephrin A1 ligand. Importantly, our data also show that different spatial densities of HT-EphA2 nanopositioned in hexagons led to other dynamic processes of ephrin A1 clustering. The number of clusters increased with time on all nanopatterns with a variety of densities, with the 60 min time point giving the highest number of ligand clusters (Figure 7D,E). Notably, the total number of clusters at the 60 min time point was influenced by the line density at the nanoscale and significantly differed between 1000 and 250 nm conditions, thus confirming the data shown in Figure 7B. Finally, we found it interesting that the total number of clusters formed on the nanopattern with line spacings of 250 nm was very similar to the total number of clusters produced on our positive control (MICRO) surface. This finding offers more support for the possibility of cell interactions in the very narrow spaces presented by the nanopatterned surface. The negative control did not give a high level of cluster formation.

Lastly, to demonstrate that ephrin A ligand-binding elicits Eph receptor/ephrin downstream signaling on nanopatterns, we analyzed the colocalization of ephrin A1 clusters with FYN kinase clusters. As shown in Figure S5A, ephrin A1 and FYN form colocalizing clusters on all tested nanopatterns, and a subsequent image analysis of the ephrin A1/FYN kinase cluster colocalization confirmed that, on all tested substrates, these two molecules specifically interact (Figure S5B). Additionally, their cluster numbers are dependent on the nanopattern density (Figure S5B), corresponding with the data shown in Figure 7B. Our observations of high colocalization of ephrin A1 and FYN clusters match with results of previous publications that show that specific ephrin A ligand spacing effectively activated EphA2 receptor function.[61,118] Our results show that ephrin ligand distribution and organization within the cell membrane and its downstream signaling can be influenced and controlled using nanopatterned EphA receptors.

CONCLUSION

Our research demonstrates that EBL can be used to create large areas of complex, high-resolution nanopatterns that are cell-culture-compatible. These nanopatterns can be used to study the localization of virtually any biomolecule and the corresponding dynamics of cell−cell interactions. Our results show that EBL can be significantly improved using several optimization steps that ensure biocompatibility with cell models, while maintaining a high resolution of nanostructures and high throughput. Furthermore, optimized EBL can be used to create a structurally complex hexagonal network of nanopatterns, thus significantly expanding the potential of current EBL methods in cell biology research. Importantly, the combination of EBL with the highly versatile HaloTag system for site-specific and covalent immobilization of recombinant proteins represents a universal and effective method to study mechanisms of cell−cell interactions in great detail. Although our results reveal a particular mechanism for spatial-mechanical regulation of specific EphA2 signaling pathways, our platform can be easily expanded to different and multiple proteins and cell lines. Thus, the technology reported herein will be universally applicable to mechanistic cell biology experiments that analyze the spatial distribution of signaling molecules and pathways. We envision that this technology will also be particularly useful in numerous practical applications, including nanobiochips and nanosensors. Knowledge of the spatial distribution of specific signaling molecules can serve as the basis for the future design of complex and biologically active three-dimensional biomaterials.

ASSOCIATED CONTENT

Supporting Information

The Supporting Information is available free of charge at https://pubs.acs.org/doi/10.1021/acsbiomaterials.2c00650.

Expression profile, MALDI-TOF analysis, L-HT-EphA2 concentration effects, nanopatterned EphA2 receptors influencing intracellular localization and clustering of ephrin A ligands of hPSCs, nanopatterned EphA2 influencing intracellular localization and clustering of ephrin A1 ligand and FYN kinase in hPSCs, list of PEG solutions, list of primers for qPCR, and a list of antibodies (PDF)

AUTHOR INFORMATION

Corresponding Author

Josef Jaros − *Department of Histology and Embryology, Faculty of Medicine, Masaryk University, Brno 625 00, Czech Republic; International Clinical Research Center (ICRC), St. Anne's University Hospital, Brno 656 91, Czech Republic;* orcid.org/0000-0001-7559-2344; Email: jaros@med.muni.cz

Authors

Jakub Pospíšil − *Department of Histology and Embryology, Faculty of Medicine, Masaryk University, Brno 625 00, Czech Republic; Core Facility Cellular Imaging, CEITEC, Masaryk University, Brno 625 00, Czech Republic;* orcid.org/0000-0002-8679-677X

Miloš Hrabovský − *TESCAN Orsay Holding a.s., Brno 623 00, Czech Republic*

Dáša Bohačiaková − *Department of Histology and Embryology, Faculty of Medicine, Masaryk University, Brno 625 00, Czech Republic; International Clinical Research Center (ICRC), St. Anne's University Hospital, Brno 656 91, Czech Republic*

Zuzana Hovádková − *TESCAN Brno s.r.o., Brno 623 00, Czech Republic;* Present Address: Z.H.: AnaPath GmbH, Schafmattweg 36, 4102 Binningen, Switzerland

Miroslav Jurásek − *TESCAN Brno s.r.o., Brno 623 00, Czech Republic*

Jarmila Mlčoušková − *Department of Biology, Faculty of Medicine, Masaryk University, Brno 625 00, Czech Republic*

Kamil Paruch − *International Clinical Research Center (ICRC), St. Anne's University Hospital, Brno 656 91, Czech Republic; Department of Chemistry, Faculty of Science, Masaryk University, Brno 625 00, Czech Republic;* orcid.org/0000-0001-9502-3173

Šárka Nevolová − *International Clinical Research Center (ICRC), St. Anne's University Hospital, Brno 656 91, Czech Republic; Loschmidt Laboratories, Department of Experimental Biology and Research Centre for Toxic*

Compounds in the Environment (RECETOX), Masaryk University, Brno 625 00, Czech Republic

Jiri Damborsky − *International Clinical Research Center (ICRC), St. Anne's University Hospital, Brno 656 91, Czech Republic; Loschmidt Laboratories, Department of Experimental Biology and Research Centre for Toxic Compounds in the Environment (RECETOX), Masaryk University, Brno 625 00, Czech Republic;* orcid.org/0000-0002-7848-8216

Aleš Hampl − *Department of Histology and Embryology, Faculty of Medicine, Masaryk University, Brno 625 00, Czech Republic; International Clinical Research Center (ICRC), St. Anne's University Hospital, Brno 656 91, Czech Republic;* orcid.org/0000-0002-8963-9235

Complete contact information is available at: https://pubs.acs.org/10.1021/acsbiomaterials.2c00650

Author Contributions

J.J. and A.H. initiated and supervised the research. M.H., Z.H., M.J., and J.P. carried out the electron-beam lithography experiments and scanning electron microscopy measurements. J.M. and J.P. carried out the atomic force microscopy measurements. Š.N. performed the MALDI-TOF analysis. J.P. and J.J. planned and carried out the cell-interaction studies, including immunofluorescence and super-resolution microscopy. J.J. and K.P. planned and carried out preparative biochemical work. J.P., J.J., A.H., J.J., K.P., and D.B. discussed and interpreted the obtained experimental data. J.P. and J.J. prepared the overall body of experimental results for publication and wrote the manuscript. J.J., D.B. and J.P. participated in critical reading of the manuscript and its improvements. All authors have given approval to the final version of the manuscript.

Notes

The authors declare no competing financial interest.

■ ACKNOWLEDGMENTS

This work was supported by the European Regional Development Fund—project INBIO (CZ.02.1.01/0.0/0.0/16_026/0008451). The authors would like to acknowledge the Ministry of Education, Youth and Sport of the Czech Republic (MEYS CR) for financial support (European Strategy Forum on Research Infrastructures [ESFRI] Research Centre for Toxic Compounds in the Environment [RECETOX] LM2018121). This project has received funding from the European Union's Horizon 2020 research and innovation program under grant agreement 857560. The article reflects the authors' views, and the agency is not responsible for any use that may be made of the information it contains. D.B. was supported by funds from Alzheimer nadační fond, Prague, Czech Republic, and by Career Restart Grant (MUNI/R/1697/2020). The authors acknowledge the core facility CELLIM supported by the Czech-BioImaging large RI project (LM2018129, funded by MEYS CR) for their support with obtaining scientific data presented in this paper. The authors gratefully acknowledge the Czech Infrastructure for Integrative Structural Biology (CIISB), the Instruct-CZ Centre of Instruct-ERIC EU consortium, funded by MEYS CR infrastructure project LM2018127, and the European Regional Development Fund project UP CIISB (CZ.02.1.01/0.0/0.0/18_046/0015974) for financial support of the experiments performed at the CF Nanobiotechnology. The authors also acknowledge the support provided by CZ-OPENSCREEN, National Infrastructure for Chemical Biology (LM2018130), and by Bader Philanthropies, Inc.

■ REFERENCES

(1) Werner, S.; Grose, R. Regulation of Wound Healing by Growth Factors and Cytokines. *Physiol. Rev.* **2003**, *83* (3), 835−870.

(2) Zamir, E.; Katz, M.; Posen, Y.; Erez, N.; Yamada, K. M.; Katz, B. Z.; Lin, S.; Lin, D. C.; Bershadsky, A.; Kam, Z.; Geiger, B. Dynamics and Segregation of Cell-Matrix Adhesions in Cultured Fibroblasts. *Nat. Cell Biol.* **2000**, *2* (4), 191−196.

(3) Suzuki, K.; Saito, J.; Yanai, R.; Yamada, N.; Chikama, T.; Seki, K.; Nishida, T. Cell-Matrix and Cell-Cell Interactions during Corneal Epithelial Wound Healing. *Prog. Retin. Eye Res.* **2003**, *22* (2), 113−133.

(4) Yao, X.; Peng, R.; Ding, J. Cell−Material Interactions Revealed Via Material Techniques of Surface Patterning. *Adv. Mater.* **2013**, *25* (37), 5257−5286.

(5) Alghisi, G.; Ponsonnet, L.; Rüegg, C. The Integrin Antagonist Cilengitide Activates AVβ3, Disrupts VE-Cadherin Localization at Cell Junctions and Enhances Permeability in Endothelial Cells. *PloS One* **2009**, *4*, e4449.

(6) Yeo, I.-S.; Min, S.-K.; Ki Kang, H.; Kwon, T.-K.; Youn Jung, S.; Min, B.-M. Adhesion and Spreading of Osteoblast-like Cells on Surfaces Coated with Laminin-Derived Bioactive Core Peptides. *Data Brief* **2015**, *5*, 411−415.

(7) Matsui, N.; Nozaki, K.; Ishihara, K.; Yamashita, K.; Nagai, A. Concentration-Dependent Effects of Fibronectin Adsorbed on Hydroxyapatite Surfaces on Osteoblast Adhesion. *Mater. Sci. Eng., C* **2015**, *48*, 378−383.

(8) Docheva, D.; Padula, D.; Schieker, M.; Clausen-Schaumann, H. Effect of Collagen I and Fibronectin on the Adhesion, Elasticity and Cytoskeletal Organization of Prostate Cancer Cells. *Biochem. Biophys. Res. Commun.* **2010**, *402* (2), 361−366.

(9) Chen, C. S.; Mrksich, M.; Huang, S.; Whitesides, G. M.; Ingber, D. E. Geometric Control of Cell Life and Death. *Science* **1997**, *276* (5317), 1425−1428.

(10) McBeath, R.; Pirone, D. M.; Nelson, C. M.; Bhadriraju, K.; Chen, C. S. Cell Shape, Cytoskeletal Tension, and RhoA Regulate Stem Cell Lineage Commitment. *Dev. Cell* **2004**, *6* (4), 483−495.

(11) Zheng, S.; Liu, Q.; He, J.; Wang, X.; Ye, K.; Wang, X.; Yan, C.; Liu, P.; Ding, J. Critical Adhesion Areas of Cells on Micro-Nanopatterns. *Nano Res.* **2022**, *15* (2), 1623−1635.

(12) Nakanishi, J.; Kikuchi, Y.; Takarada, T.; Nakayama, H.; Yamaguchi, K.; Maeda, M. Spatiotemporal Control of Cell Adhesion on a Self-Assembled Monolayer Having a Photocleavable Protecting Group. *Anal. Chim. Acta* **2006**, *578* (1), 100−104.

(13) Albert, P. J.; Schwarz, U. S. Modeling Cell Shape and Dynamics on Micropatterns. *Cell Adhes. Migr.* **2016**, *10* (5), 516−528.

(14) Théry, M.; Racine, V.; Piel, M.; Pépin, A.; Dimitrov, A.; Chen, Y.; Sibarita, J.-B.; Bornens, M. Anisotropy of Cell Adhesive Microenvironment Governs Cell Internal Organization and Orientation of Polarity. *Proc. Natl. Acad. Sci. U. S. A.* **2006**, *103* (52), 19771−19776.

(15) Kikuchi, Y.; Nakanishi, J.; Nakayama, H.; Shimizu, T.; Yoshino, Y.; Yamaguchi, K.; Yoshida, Y.; Horiike, Y. Grafting Poly(Ethylene Glycol) to a Glass Surface via a Photocleavable Linker for Light-Induced Cell Micropatterning and Cell Proliferation Control. *Chem. Lett.* **2008**, *37* (10), 1062−1063.

(16) Deglincerti, A.; Etoc, F.; Guerra, M. C.; Martyn, I.; Metzger, J.; Ruzo, A.; Simunovic, M.; Yoney, A.; Brivanlou, A. H.; Siggia, E.; Warmflash, A. Self-Organization of Human Embryonic Stem Cells on Micropatterns. *Nat. Protoc.* **2016**, *11* (11), 2223−2232.

(17) Geiger, B.; Spatz, J. P.; Bershadsky, A. D. Environmental Sensing through Focal Adhesions. *Nat. Rev. Mol. Cell Biol.* **2009**, *10* (1), 21−33.

(18) Dalby, M. J.; Gadegaard, N.; Oreffo, R. O. C. Harnessing Nanotopography and Integrin−Matrix Interactions to Influence Stem Cell Fate. *Nat. Mater.* **2014**, *13* (6), 558−569.
(19) Ermis, M.; Antmen, E.; Hasirci, V. Micro and Nanofabrication Methods to Control Cell-Substrate Interactions and Cell Behavior: A Review from the Tissue Engineering Perspective. *Bioact. Mater.* **2018**, *3* (3), 355−369.
(20) Humenik, M.; Winkler, A.; Scheibel, T. Patterning of Protein-Based Materials. *Biopolymers* **2021**, *112* (2), e23412.
(21) Tudureanu, R.; Handrea-Dragan, I. M.; Boca, S.; Botiz, I. Insight and Recent Advances into the Role of Topography on the Cell Differentiation and Proliferation on Biopolymeric Surfaces. *Int. J. Mol. Sci.* **2022**, *23* (14), 7731.
(22) Valiokas, R. Nanobiochips. *Cell. Mol. Life Sci.* **2012**, *69* (3), 347−356.
(23) Sadana, A.; Sadana, N.; Sadana, R. Nanobiosensors. In *A Fractal Analysis of Chemical Kinetics with Applications to Biological and Biosensor Interfaces*; Sadana, A., Sadana, N., Sadana, R., Eds.; Elsevier, 2018; Chapter 4, pp 69−96. DOI: 10.1016/B978-0-444-63872-4.00004-X.
(24) Aguilar, Z. P. Nanobiosensors. In *Nanomaterials for Medical Applications*; Aguilar, Z. P., Ed.; Elsevier, 2013; Chapter 4, pp 127−179. DOI: 10.1016/B978-0-12-385089-8.00004-2.
(25) Vigneswaran, N.; Samsuri, F.; Ranganathan, B.; Padmapriya. Recent Advances in Nano Patterning and Nano Imprint Lithography for Biological Applications. *Procedia Eng.* **2014**, *97*, 1387−1398.
(26) Wilson, D. L.; Martin, R.; Hong, S.; Cronin-Golomb, M.; Mirkin, C. A.; Kaplan, D. L. Surface Organization and Nanopatterning of Collagen by Dip-Pen Nanolithography. *Proc. Natl. Acad. Sci. U. S. A.* **2001**, *98* (24), 13660−13664.
(27) Lee, K.-B.; Park, S.-J.; Mirkin, C. A.; Smith, J. C.; Mrksich, M. Protein Nanoarrays Generated By Dip-Pen Nanolithography. *Science* **2002**, *295* (5560), 1702−1705.
(28) Hong, S.; Zhu, J.; Mirkin, C. A. Multiple Ink Nanolithography: Toward a Multiple-Pen Nano-Plotter. *Science* **1999**, *286* (5439), 523−525.
(29) Salaita, K.; Wang, Y.; Mirkin, C. A. Applications of Dip-Pen Nanolithography. *Nat. Nanotechnol.* **2007**, *2* (3), 145−155.
(30) Krivoshapkina, Y.; Kaestner, M.; Rangelow, I. W. Tip-Based Nanolithography Methods and Materials. In *Frontiers of Nanoscience*; Robinson, A., Lawson, R., Eds.; Materials and Processes for Next Generation Lithography; Elsevier, 2016; Vol. *11*, Chapter 15, pp 497−542. DOI: 10.1016/B978-0-08-100354-1.00015-6.
(31) Giam, L. R.; Massich, M. D.; Hao, L.; Wong, L. S.; Mader, C. C.; Mirkin, C. A. Scanning Probe-Enabled Nanocombinatorics Define the Relationship between Fibronectin Feature Size and Stem Cell Fate. *Proc. Natl. Acad. Sci. U. S. A.* **2012**, *109* (12), 4377−4382.
(32) Liu, G. Y.; Xu, S.; Qian, Y. Nanofabrication of Self-Assembled Monolayers Using Scanning Probe Lithography. *Acc. Chem. Res.* **2000**, *33* (7), 457−466.
(33) Shi, J.; Chen, J.; Cremer, P. S. Sub-100 Nm Patterning of Supported Bilayers by Nanoshaving Lithography. *J. Am. Chem. Soc.* **2008**, *130* (9), 2718−2719.
(34) Kenseth, J. R.; Harnisch, J. A.; Jones, V. W.; Porter, M. D. Investigation of Approaches for the Fabrication of Protein Patterns by Scanning Probe Lithography. *Langmuir* **2001**, *17* (13), 4105−4112.
(35) ElZubir, O.; Barlow, I.; Leggett, G. J.; Williams, N. H. Fabrication of Molecular Nanopatterns at Aluminium Oxide Surfaces by Nanoshaving of Self-Assembled Monolayers of Alkylphosphonates. *Nanoscale* **2013**, *5* (22), 11125−11131.
(36) Liu, M.; Amro, N. A.; Liu, G. Nanografting for Surface Physical Chemistry. *Annu. Rev. Phys. Chem.* **2008**, *59*, 367−386.
(37) Garcia-Cruz, A.; Lee, M.; Zine, N.; Sigaud, M.; Marote, P.; Lopez, M.; Bausells, J.; Jaffrezic-Renault, N.; Errachid, A. Biopatterning of Antibodies on Poly(Pyrrole)-Nanowires Using Nanocontact Printing: Surface Characterization. *Mater. Sci. Eng., C* **2018**, *91*, 466−474.
(38) Li, H.-W.; Muir, B. V. O.; Fichet, G.; Huck, W. T. S. Nanocontact Printing: A Route to Sub-50-Nm-Scale Chemical and Biological Patterning. *Langmuir* **2003**, *19* (6), 1963−1965.
(39) Renault, J. P.; Bernard, A.; Bietsch, A.; Michel, B.; Bosshard, H. R.; Delamarche, E.; Kreiter, M.; Hecht, B.; Wild, U. P. Fabricating Arrays of Single Protein Molecules on Glass Using Microcontact Printing. *J. Phys. Chem. B* **2003**, *107* (3), 703−711.
(40) Kolodziej, C. M.; Maynard, H. D. Electron-Beam Lithography for Patterning Biomolecules at the Micron and Nanometer Scale. *Chem. Mater.* **2012**, *24* (5), 774−780.
(41) Vieu, C.; Carcenac, F.; Pépin, A.; Chen, Y.; Mejias, M.; Lebib, A.; Manin-Ferlazzo, L.; Couraud, L.; Launois, H. Electron Beam Lithography: Resolution Limits and Applications. *Appl. Surf. Sci.* **2000**, *164* (1), 111−117.
(42) Lercel, M. J.; Whelan, C. S.; Craighead, H. G.; Seshadri, K.; Allara, D. L. High-resolution Silicon Patterning with Self-assembled Monolayer Resists. *J. Vac. Sci. Technol. B Microelectron. Nanometer Struct. Process. Meas. Phenom.* **1996**, *14* (6), 4085−4090.
(43) Zhang, G.-J.; Tanii, T.; Funatsu, T.; Ohdomari, I. Patterning of DNA Nanostructures on Silicon Surface by Electron Beam Lithography of Self-Assembled Monolayer. *Chem. Commun.* **2004**, No. 7, 786−787.
(44) Lussi, J. W.; Tang, C.; Kuenzi, P.-A.; Staufer, U.; Csucs, G.; Vörös, J.; Danuser, G.; Hubbell, J. A.; Textor, M. Selective Molecular Assembly Patterning at the Nanoscale: A Novel Platform for Producing Protein Patterns by Electron-Beam Lithography on SiO2/Indium Tin Oxide-Coated Glass Substrates. *Nanotechnology* **2005**, *16* (9), 1781−1786.
(45) Künzi, P. A.; Lussi, J.; Aeschimann, L.; Danuser, G.; Textor, M.; de Rooij, N. F.; Staufer, U. Nanofabrication of Protein-Patterned Substrates for Future Cell Adhesion Experiments. *Microelectron. Eng.* **2005**, *78*−*79*, 582−586.
(46) Park, M.; Harrison, C.; Chaikin, P. M.; Register, R. A.; Adamson, D. H. Block Copolymer Lithography: Periodic Arrays of ∼ 1011 Holes in 1 Square Centimeter. *Science* **1997**, *276* (5317), 1401−1404.
(47) Jo, K.; Teague, S.; Chen, B.; Khan, H. A.; Freeburne, E.; Li, H.; Li, B.; Ran, R.; Spence, J. R.; Heemskerk, I. Efficient Differentiation of Human Primordial Germ Cells through Geometric Control Reveals a Key Role for Nodal Signaling. *eLife* **2022**, *11*, e72811.
(48) Irvine, D. J.; Mayes, A. M.; Griffith, L. G. Nanoscale Clustering of RGD Peptides at Surfaces Using Comb Polymers. 1. Synthesis and Characterization of Comb Thin Films. *Biomacromolecules* **2001**, *2* (1), 85−94.
(49) Lau, U. Y.; Saxer, S. S.; Lee, J.; Bat, E.; Maynard, H. D. Direct Write Protein Patterns for Multiplexed Cytokine Detection from Live Cells Using Electron Beam Lithography. *ACS Nano* **2016**, *10* (1), 723−729.
(50) Zhang, M.; Desai, T.; Ferrari, M. Proteins and Cells on PEG Immobilized Silicon Surfaces. *Biomaterials* **1998**, *19* (10), 953−960.
(51) Yates, N.; Fascione, M.; Parkin, A. Methodologies for "Wiring" Redox Proteins/Enzymes to Electrode Surfaces. *Chemistry* **2018**, *24* (47), 12164−12182.
(52) Hutsell, S. Q.; Kimple, R. J.; Siderovski, D. P.; Willard, F. S.; Kimple, A. J. High Affinity Immobilization of Proteins Using Biotin- and GST-Based Coupling Strategies. *Methods Mol. Biol. Clifton NJ.* **2010**, *627*, 75−90.
(53) Lutolf, M. p.; Raeber, G. p.; Zisch, A. h.; Tirelli, N.; Hubbell, J. a. Cell-Responsive Synthetic Hydrogels. *Adv. Mater.* **2003**, *15* (11), 888−892.
(54) Taniguchi, Y.; Kawakami, M. Application of HaloTag Protein to Covalent Immobilization of Recombinant Proteins for Single Molecule Force Spectroscopy. *Langmuir* **2010**, *26* (13), 10433−10436.
(55) Grainger, D. W.; Castner, D. G.; Dubey, M.; Emoto, K.; Takahashi, H. Affinity-Based Protein Surface Pattern Formation by Ligand Self-Selection from Mixed Protein Solutions. *Adv. Funct. Mater.* **2009**, *19* (19), 3046−3055.

(56) Benink, H.; Urh, M. HaloTag Technology for Specific and Covalent Labeling of Fusion Proteins. *Methods Mol. Biol. Clifton NJ.* **2015**, *1266*, 119−128.
(57) Wang, X.; Li, S.; Yan, C.; Liu, P.; Ding, J. Fabrication of RGD Micro/Nanopattern and Corresponding Study of Stem Cell Differentiation. *Nano Lett.* **2015**, *15* (3), 1457−1467.
(58) Chen, Z.; Oh, D.; Biswas, K. H.; Zaidel-Bar, R.; Groves, J. T. Probing the Effect of Clustering on EphA2 Receptor Signaling Efficiency by Subcellular Control of Ligand-Receptor Mobility. *eLife* **2021**, *10*, e67379.
(59) Davy, A.; Soriano, P. Ephrin Signaling in Vivo: Look Both Ways. *Dev. Dyn.* **2005**, *232* (1), 1−10.
(60) Genander, M.; Frisén, J. Ephrins and Eph Receptors in Stem Cells and Cancer. *Curr. Opin. Cell Biol.* **2010**, *22* (5), 611−616.
(61) Shaw, A.; Lundin, V.; Petrova, E.; Fördős, F.; Benson, E.; Al-Amin, A.; Herland, A.; Blokzijl, A.; Högberg, B.; Teixeira, A. I. Spatial Control of Membrane Receptor Function Using Ligand Nanocalipers. *Nat. Methods* **2014**, *11* (8), 841−846.
(62) Lai, D.; Wang, Y.; Sun, J.; Chen, Y.; Li, T.; Wu, Y.; Guo, L.; Wei, C. Derivation and Characterization of Human Embryonic Stem Cells on Human Amnion Epithelial Cells. *Sci. Rep.* **2015**, *5* (1), 10014.
(63) Baltzis, K. Hexagonal vs Circular Cell Shape: A Comparative Analysis and Evaluation of the Two Popular Modeling Approximations. In *Cellular Networks*; IntechOpen, 2011. DOI: 10.5772/14851.
(64) Altissimo, M. E-Beam Lithography for Micro-/nanofabrication. *Biomicrofluidics* **2010**, *4* (2), 026503.
(65) Porokh, V.; Vaňhara, P.; Bárta, T.; Jurečková, L.; Bohačiaková, D.; Pospíšilová, V.; Mináriková, D.; Holubcová, Z.; Pelková, V.; Souček, K.; Hampl, A. Soluble Cripto-1 Induces Accumulation of Supernumerary Centrosomes and Formation of Aberrant Mitoses in Human Embryonic Stem Cells. *Stem Cells Dev.* **2018**, *27* (16), 1077−1084.
(66) Pospíšilová, V.; Ešner, M.; Červenková, I.; Fedr, R.; Tinevez, J.-Y.; Hampl, A.; Anger, M. The Frequency and Consequences of Multipolar Mitoses in Undifferentiated Embryonic Stem Cells. *J. Appl. Biomed.* **2019**, *17* (4), 209−217.
(67) Fedorova, V.; Vanova, T.; Elrefae, L.; Pospisil, J.; Petrasova, M.; Kolajova, V.; Hudacova, Z.; Baniariova, J.; Barak, M.; Peskova, L.; Barta, T.; Kaucka, M.; Killinger, M.; Vecera, J.; Bernatik, O.; Cajanek, L.; Hribkova, H.; Bohaciakova, D. Differentiation of Neural Rosettes from Human Pluripotent Stem Cells in Vitro Is Sequentially Regulated on a Molecular Level and Accomplished by the Mechanism Reminiscent of Secondary Neurulation. *Stem Cell Res.* **2019**, *40*, 101563.
(68) Asano, S. M.; Gao, R.; Wassie, A. T.; Tillberg, P.; Chen, F.; Boyden, E. S. Expansion Microscopy: Protocols for Imaging Proteins and RNA in Cells and Tissues. *Curr. Protoc. Cell Biol.* **2018**, *80* (1), e56.
(69) Schindelin, J.; Arganda-Carreras, I.; Frise, E.; Kaynig, V.; Longair, M.; Pietzsch, T.; Preibisch, S.; Rueden, C.; Saalfeld, S.; Schmid, B.; Tinevez, J.-Y.; White, D. J.; Hartenstein, V.; Eliceiri, K.; Tomancak, P.; Cardona, A. Fiji: An Open-Source Platform for Biological-Image Analysis. *Nat. Methods* **2012**, *9* (7), 676−682.
(70) Tseng, A.A.; Chen, K.; Chen, C.D.; Ma, K.J. Electron Beam Lithography in Nanoscale Fabrication: Recent Development. *IEEE Trans. Electron. Packag. Manuf.* **2003**, *26* (2), 141−149.
(71) Groves, T. R. Electron Beam Lithography. In *Nanolithography*; Feldman, M., Ed.; Woodhead Publishing, 2014; Chapter 3, pp 80−115. DOI: 10.1533/9780857098757.80.
(72) Lee, M.-H.; Kim, H.-M.; Cho, S.-Y.; Lim, K.; Park, S.-Y.; Jong Lee, J.; Kim, K.-B. Fabrication of Ultra-High-Density Nanodot Array Patterns (∼3 Tbits/in.2) Using Electron-Beam Lithography. *J. Vac. Sci. Technol. B* **2011**, *29* (6), 061602.
(73) Grigorescu, A.; Hagen, C. W. Resists for Sub-20-Nm Electron Beam Lithography with a Focus on HSQ: State of the Art. *Nanotechnology* **2009**, *20*, 292001.
(74) Lin, J.-J.; Li, Z.-Q. Electronic Conduction Properties of Indium Tin Oxide: Single-Particle and Many-Body Transport. *J. Phys. Condens. Matter Inst. Phys. J.* **2014**, *26* (34), 343201.
(75) Kim, H.; Gilmore, C. M.; Piqué, A.; Horwitz, J. S.; Mattoussi, H.; Murata, H.; Kafafi, Z. H.; Chrisey, D. B. Electrical, Optical, and Structural Properties of Indium−Tin−Oxide Thin Films for Organic Light-Emitting Devices. *J. Appl. Phys.* **1999**, *86* (11), 6451−6461.
(76) Lichtenberg, J. Y.; Ling, Y.; Kim, S. Non-Specific Adsorption Reduction Methods in Biosensing. *Sensors* **2019**, *19* (11), 2488.
(77) Han, S.; Kim, C.; Kwon, D. Thermal Degradation of Poly(Ethyleneglycol). *Polym. Degrad. Stab.* **1995**, *47* (2), 203−208.
(78) Elzouka, M.; Ndao, S. High Temperature Near-Field NanoThermoMechanical Rectification. *Sci. Rep.* **2017**, *7* (1), 44901.
(79) van Zanten, T. S.; Cambi, A.; Koopman, M.; Joosten, B.; Figdor, C. G.; Garcia-Parajo, M. F. Hotspots of GPI-Anchored Proteins and Integrin Nanoclusters Function as Nucleation Sites for Cell Adhesion. *Proc. Natl. Acad. Sci. U. S. A.* **2009**, *106* (44), 18557−18562.
(80) Palmer, A.; Klein, R. Multiple Roles of Ephrins in Morphogenesis, Neuronal Networking, and Brain Function. *Genes Dev.* **2003**, *17* (12), 1429−1450.
(81) Sur, M.; Rubenstein, J. L. R. Patterning and Plasticity of the Cerebral Cortex. *Science* **2005**, *310* (5749), 805−810.
(82) Nikolov, D. B.; Xu, K.; Himanen, J. P. Eph/Ephrin Recognition and the Role of Eph/Ephrin Clusters in Signaling Initiation. *Biochim. Biophys. Acta* **2013**, *1834* (10), 2160−2165.
(83) Ravasio, A.; Myaing, M. Z.; Chia, S.; Arora, A.; Sathe, A.; Cao, E. Y.; Bertocchi, C.; Sharma, A.; Arasi, B.; Chung, V. Y.; Greene, A. C.; Tan, T. Z.; Chen, Z.; Ong, H. T.; Iyer, N. G.; Huang, R. Y.; DasGupta, R.; Groves, J. T.; Viasnoff, V. Single-Cell Analysis of EphA Clustering Phenotypes to Probe Cancer Cell Heterogeneity. *Commun. Biol.* **2020**, *3* (1), 1−12.
(84) Singh, D. R.; Kanvinde, P.; King, C.; Pasquale, E. B.; Hristova, K. The EphA2 Receptor Is Activated through Induction of Distinct, Ligand-Dependent Oligomeric Structures. *Commun. Biol.* **2018**, *1* (1), 1−12.
(85) Irie, N.; Takada, Y.; Watanabe, Y.; Matsuzaki, Y.; Naruse, C.; Asano, M.; Iwakura, Y.; Suda, T.; Matsuo, K. Bidirectional Signaling through EphrinA2-EphA2 Enhances Osteoclastogenesis and Suppresses Osteoblastogenesis. *J. Biol. Chem.* **2009**, *284* (21), 14637−14644.
(86) Rundle, C. H.; Xing, W.; Lau, K.-H. W.; Mohan, S. Bidirectional Ephrin Signaling in Bone. *Osteoporos. Sarcopenia* **2016**, *2* (2), 65−76.
(87) Eph Nomenclature Committee. Unified Nomenclature for Eph Family Receptors and Their Ligands, the Ephrins. *Cell* **1997**, *90* (3), 403−404.
(88) Casanova, M. R.; Reis, R. L.; Martins, A.; Neves, N. M. Surface Biofunctionalization to Improve the Efficacy of Biomaterial Substrates to Be Used in Regenerative Medicine. *Mater. Horiz.* **2020**, *7* (9), 2258−2275.
(89) Wong, L. S.; Karthikeyan, C. V.; Eichelsdoerfer, D. J.; Micklefield, J.; Mirkin, C. A. A Methodology for Preparing Nanostructured Biomolecular Interfaces with High Enzymatic Activity. *Nanoscale* **2012**, *4* (2), 659−666.
(90) Wagner, H.; Li, Y.; Hirtz, M.; Chi, L.; Fuchs, H.; Studer, A. Site Specific Protein Immobilization into Structured Polymer Brushes Prepared by AFM Lithography. *Soft Matter* **2011**, *7* (21), 9854−9858.
(91) Salaita, K.; Nair, P. M.; Petit, R. S.; Neve, R. M.; Das, D.; Gray, J. W.; Groves, J. T. Restriction of Receptor Movement Alters Cellular Response: Physical Force Sensing by EphA2. *Science* **2010**, *327* (5971), 1380−1385.
(92) Chen, K. G.; Mallon, B. S.; McKay, R. D. G.; Robey, P. G. Human Pluripotent Stem Cell Culture: Considerations for Maintenance, Expansion, and Therapeutics. *Cell Stem Cell* **2014**, *14* (1), 13−26.
(93) Nebe, B.; Finke, B.; Körtge, A.; Rebl, H.; Staehlke, S. Geometrical Micropillars Combined with Chemical Surface Mod-

https://doi.org/10.1021/acsbiomaterials.2c00650
ACS Biomater. Sci. Eng. 2022, 8, 4789−4806

ifications - Independency of Actin Filament Spatial Distribution in Primary Osteoblasts. *Mater. Sci. Forum* **2014**, *783*−*786*, 1320−1325.
(94) Singh, A.; Winterbottom, E.; Daar, I. O. Eph/Ephrin Signaling in Cell-Cell and Cell-Substrate Adhesion. *Front. Biosci. Landmark Ed.* **2012**, *17*, 473−497.
(95) Xu, Q.; Lin, W.-C.; Petit, R. S.; Groves, J. T. EphA2 Receptor Activation by Monomeric Ephrin-A1 on Supported Membranes. *Biophys. J.* **2011**, *101* (11), 2731−2739.
(96) Wakao, S.; Kitada, M.; Kuroda, Y.; Ogura, F.; Murakami, T.; Niwa, A.; Dezawa, M. Morphologic and Gene Expression Criteria for Identifying Human Induced Pluripotent Stem Cells. *PloS One* **2012**, *7*, e48677.
(97) Prager-Khoutorsky, M.; Lichtenstein, A.; Krishnan, R.; Rajendran, K.; Mayo, A.; Kam, Z.; Geiger, B.; Bershadsky, A. D. Fibroblast Polarization Is a Matrix-Rigidity-Dependent Process Controlled by Focal Adhesion Mechanosensing. *Nat. Cell Biol.* **2011**, *13* (12), 1457−1465.
(98) Gauthier, N. C.; Masters, T. A.; Sheetz, M. P. Mechanical Feedback between Membrane Tension and Dynamics. *Trends Cell Biol.* **2012**, *22* (10), 527−535.
(99) Wang, X.; Hu, X.; Dulińska-Molak, I.; Kawazoe, N.; Yang, Y.; Chen, G. Discriminating the Independent Influence of Cell Adhesion and Spreading Area on Stem Cell Fate Determination Using Micropatterned Surfaces. *Sci. Rep.* **2016**, *6* (1), 28708.
(100) Cabezas, M. D.; Meckes, B.; Mirkin, C. A.; Mrksich, M. Subcellular Control over Focal Adhesion Anisotropy, Independent of Cell Morphology, Dictates Stem Cell Fate. *ACS Nano* **2019**, *13* (10), 11144−11152.
(101) Min, S.; Jeon, Y. S.; Choi, H.; Khatua, C.; Li, N.; Bae, G.; Jung, H. J.; Kim, Y.; Hong, H.; Shin, J.; Ko, M. J.; Ko, H. S.; Kim, T.; Moon, J. H.; Song, J.-J.; Dravid, V. P.; Kim, Y. K.; Kang, H. Large and Externally Positioned Ligand-Coated Nanopatches Facilitate the Adhesion-Dependent Regenerative Polarization of Host Macrophages. *Nano Lett.* **2020**, *20* (10), 7272−7280.
(102) Pallarola, D.; Bochen, A.; Guglielmotti, V.; Oswald, T. A.; Kessler, H.; Spatz, J. P. Highly Ordered Gold Nanopatterned Indium Tin Oxide Electrodes for Simultaneous Optical and Electrochemical Probing Cell Interactions. *Anal. Chem.* **2017**, *89* (18), 10054−10062.
(103) Wong, S. H. D.; Xu, X.; Chen, X.; Xin, Y.; Xu, L.; Lai, C. H. N.; Oh, J.; Wong, W. K. R.; Wang, X.; Han, S.; You, W.; Shuai, X.; Wong, N.; Tan, Y.; Duan, L.; Bian, L. Manipulation of the Nanoscale Presentation of Integrin Ligand Produces Cancer Cells with Enhanced Stemness and Robust Tumorigenicity. *Nano Lett.* **2021**, *21* (7), 3225−3236.
(104) Chu, M.; Zhang, C. Inhibition of Angiogenesis by Leflunomide via Targeting the Soluble Ephrin-A1/EphA2 System in Bladder Cancer. *Sci. Rep.* **2018**, *8* (1), 1539.
(105) Funk, S. D.; Yurdagul, A.; Albert, P.; Traylor, J. G.; Jin, L.; Chen, J.; Orr, A. W. EphA2 Activation Promotes the Endothelial Cell Inflammatory Response: A Potential Role in Atherosclerosis. *Arterioscler. Thromb. Vasc. Biol.* **2012**, *32* (3), 686−695.
(106) Wakayama, Y.; Miura, K.; Sabe, H.; Mochizuki, N. EphrinA1-EphA2 Signal Induces Compaction and Polarization of Madin-Darby Canine Kidney Cells by Inactivating Ezrin through Negative Regulation of RhoA. *J. Biol. Chem.* **2011**, *286* (51), 44243−44253.
(107) Wykosky, J.; Debinski, W. The EphA2 Receptor and EphrinA1 Ligand in Solid Tumors: Function and Therapeutic Targeting. *Mol. Cancer Res. MCR* **2008**, *6* (12), 1795−1806.
(108) Balatskaya, M. N.; Baglay, A. I.; Rubtsov, Y. P.; V Sharonov, G. Analysis of GPI-Anchored Receptor Distribution and Dynamics in Live Cells by Tag-Mediated Enzymatic Labeling and FRET. *Methods Protoc.* **2020**, *3* (2), 33.
(109) Tillberg, P. W.; Chen, F.; Piatkevich, K. D.; Zhao, Y.; Yu, C.-C. J.; English, B. P.; Gao, L.; Martorell, A.; Suk, H.-J.; Yoshida, F.; DeGennaro, E. M.; Roossien, D. H.; Gong, G.; Seneviratne, U.; Tannenbaum, S. R.; Desimone, R.; Cai, D.; Boyden, E. S. Protein-Retention Expansion Microscopy of Cells and Tissues Labeled Using Standard Fluorescent Proteins and Antibodies. *Nat. Biotechnol.* **2016**, *34* (9), 987−992.
(110) Seiradake, E.; Harlos, K.; Sutton, G.; Aricescu, A. R.; Jones, E. Y. An Extracellular Steric Seeding Mechanism for Eph-Ephrin Signaling Platform Assembly. *Nat. Struct. Mol. Biol.* **2010**, *17* (4), 398−402.
(111) Himanen, J. P.; Yermekbayeva, L.; Janes, P. W.; Walker, J. R.; Xu, K.; Atapattu, L.; Rajashankar, K. R.; Mensinga, A.; Lackmann, M.; Nikolov, D. B.; Dhe-Paganon, S. Architecture of Eph Receptor Clusters. *Proc. Natl. Acad. Sci. U. S. A.* **2010**, *107* (24), 10860−10865.
(112) Baba, A.; Akagi, K.; Takayanagi, M.; Flanagan, J. G.; Kobayashi, T.; Hattori, M. Fyn Tyrosine Kinase Regulates the Surface Expression of Glycosylphosphatidylinositol-Linked Ephrin via the Modulation of Sphingomyelin Metabolism. *J. Biol. Chem.* **2009**, *284* (14), 9206−9214.
(113) Davy, A.; Gale, N. W.; Murray, E. W.; Klinghoffer, R. A.; Soriano, P.; Feuerstein, C.; Robbins, S. M. Compartmentalized Signaling by GPI-Anchored Ephrin-A5 Requires the Fyn Tyrosine Kinase to Regulate Cellular Adhesion. *Genes Dev.* **1999**, *13* (23), 3125−3135.
(114) Changede, R.; Cai, H.; Wind, S. J.; Sheetz, M. P. Integrin Nanoclusters Can Bridge Thin Matrix Fibres to Form Cell−Matrix Adhesions. *Nat. Mater.* **2019**, *18* (12), 1366−1375.
(115) Huai, J.; Drescher, U. An Ephrin-A-Dependent Signaling Pathway Controls Integrin Function and Is Linked to the Tyrosine Phosphorylation of a 120-KDa Protein. *J. Biol. Chem.* **2001**, *276* (9), 6689−6694.
(116) Verheyen, T.; Fang, T.; Lindenhofer, D.; Wang, Y.; Akopyan, K.; Lindqvist, A.; Högberg, B.; Teixeira, A. I. Spatial Organization-Dependent EphA2 Transcriptional Responses Revealed by Ligand Nanocalipers. *Nucleic Acids Res.* **2020**, *48* (10), 5777−5787.

https://doi.org/10.1021/acsbiomaterials.2c00650
ACS Biomater. Sci. Eng. 2022, 8, 4789−4806